University of Bristol

School of Physics

Oxygen–Lithium Functionalisation of Boron-Doped C(110) Diamond for Low-Work Function NEA Surfaces

Joseph Hynam

MSci Physics with Industrial Experience

Supervisor: Pr. Neil Fox

Advisor: Dr. Jude Laverock

Word Count: 9254

April 13, 2026

Declaration

All data presented in this report was collected by myself and my lab partner, with the exception of the reference C(100) diamond expected surface components and corresponding binding energies, taken from the 2026 publication by Ramiz Zulkharnay *et al.* and referenced throughout as a key comparison for our C(110) findings. CasaXPS was used for all XPS peak fitting and spectral analysis, while Python was used to generate the work function distribution histograms, UPS spectra, and core-level spectral shift plots presented in this report.

The MPCVD growth of all C(110) samples was carried out with the assistance of Liam Cullingford and the NanoESCA system was operated with guidance from our advisor, Dr Jude Laverock, who kindly provided us with MatLab-produced work function variation maps.

In terms of how work was divided between my lab partner and myself, we both played an equal role in sample preparation, data collection, analysis, and interpretation throughout. Specific tasks such as XPS fitting, Python plotting, and poster development efforts were shared, with regular discussion and interpretation at every stage.

AI Declaration

As part of the research described above, AI tools (ChatGPT and Claude AI) were used to generate small sections of computer code, highlight grammatical errors in some areas of the report, and assist with latex formatting, in accordance with the Project Unit's AI-use policy. These tools were used to support data analysis and to improve the communication of ideas where appropriate, and all AI-assisted code generation is documented in the accompanying notebook. Regardless of this assistance, all content presented in this report was gathered through my own research and written in my own words.

Acknowledgments

I would like to thank my supervisor, Pr. Neil Fox, for his guidance throughout this project and for consistently providing useful resources and ideas whenever they were needed. I am also incredibly grateful to the NanoESCA manager and our advisor Dr. Jude Laverock, for his explanations of the NanoESCA system, key underlying concepts, and the countless hours he set aside for us to share his expertise.

I must also thank Liam Cullingford for his assistance with MPCVD growth of all surfaces during the early stages of the project, and to Ramiz Zulkharnay for providing the basis for the XPS fitting methodology and the reference C(100) data that this work is compared against throughout.

Finally, I would like to thank my lab partner, Sophie Kelly, whose enthusiasm and input throughout was invaluable. We brainstormed ideas at every stage, working well as a team and, in doing so, I grew to feel genuine passion for our research.

Contents

Abstract

Diamond is investigated in this work due to its ultra-wide bandgap and the control of its electronic properties through chemical termination, yet the C(110) orientation remains comparatively unexplored. This work focusses on the growth and characterisation of boron-doped single-crystal C(110) diamond functionalised via molecular oxygen treatment and lithium deposition, with a non-evaporable getter (NEG) pump installed to remove water vapour during ultra-high vacuum preparation. Two MPCVD-grown samples were analysed by XPS, EF-PEEM, UPS, and SPA-LEED. H-terminated C(110) yielded $\phi \approx 3.59\,\text{eV}$ and $\chi \approx -1.00\,\text{eV}$ (averaged across two samples) with high degree of spatial uniformity ($\sigma = 0.02$ eV). Three oxygen–lithium cycles reduced ϕ to 3.01 eV and increased χ to $-1.49\,\text{eV}$, achieving a C–O–Li fraction of 54.3%, higher than previously reported on lithiated C(100), though C–O–Li bonding appeared to saturate after the second cycle. These results establish C(110) as a competitive surface for producing thermally stable, low work function negative electron affinity surfaces for vacuum electronic devices

1 Introduction

Controlled electron emission supports a range of compact energy harvesting technologies including vacuum electronic devices commonly operating as photocathodes or thermionic energy converters (TECs) [1, 2]. Emission occurs when electrons receive enough energy to overcome the material's surface barrier, characterised by the work function [3]. Since the work function is not a fixed bulk property, the efficiency of this process depends on both the material and its surface condition [3].

Conventional thermionic cathodes typically use refractory metals such as tungsten (W) and molybdenum (Mo). These materials have high work functions in the $4 - 5\,\text{eV}$ range and require operating temperatures above $\sim 1500\,\text{K}$ to reach practical charge carrier densities [2, 4]. Such temperatures accelerate surface degradation through evaporation and contamination, weakening emission performance over time [3]. The development of low work function emission surfaces that remain stable under high temperatures and vacuum is therefore a central challenge for next-generation energy harvesting technologies.

Diamond is an attractive candidate for emission applications due to its ultra-wide bandgap ($\sim$ 5.47eV), high thermal conductivity, mechanical strength and radiation tolerance [2, 5, 6]. For adequately doped and surface-engineered diamond, thermionic emission can begin near 500^oC, far below the temperatures required by metal cathodes, reducing thermally driven surface degradation and relaxing operational limits [7]. Crucially, diamond's electronic surface barrier can be engineered through chemical termination. Depending on the termination species, the work function and electron affinity can be tuned over several eV, a degree of control difficult to achieve with metals [8, 9, 10].

An important property in diamond surfaces is negative electron affinity (NEA), where the vacuum level sits below the conduction band minimum (CBM), so electrons reaching the CBM face no energy barrier to escape into vacuum [10]. Hydrogen(H)-terminated diamond is the most widely studied route to NEA, with values as negative as $-1.3\,\text{eV}$ reported on the C(100) [10, 11]. However, hydrogen desorbs above $\sim 700^o$C, and NEA is further degraded by air exposure to oxidising species such as oxygen and hydroxyl groups, making this termination unsuitable for high-temperature and long-term vacuum applications [2, 7, 12].

The thermal instability of H-termination has motivated extensive work on alternative terminations. Oxygen-metal terminations are of particular interest, as oxidation provides atmospheric stability and greater resistance to degradation than H-termination [13]. Oxygen alone produces positive electron affinity (PEA), but subsequent deposition of a metal with very low electronegativity such as lithium can form a strong surface dipole that restores and even enhances NEA compared to H-termination [9, 10]. Recent work by Zulkharnay *et al.* at the University of Bristol confirmed that a molecular O_2 oxidation method on C(100) achieved $\sim$90% effective oxygen coverage, and following lithium deposition, produced an NEA of ($-1.68\,\text{eV}$), outperforming the typical UV-ozone method ($-1.31\,\text{eV}$)) and showing full recoverability after reactivation [13].

Despite this progress, most NEA studies have focused on C(100) and C(111). The C(110) orientation has received comparatively less attention due to the challenges associated with its growth, preparation and surface reconstruction [14, 15, 16]. However, C(110) presents a distinct atomic arrangement that may support stable coexisting ketone (C=O) and ether (C-O-C) oxygen configurations during functionalisation, potentially offering favourable conditions for lithium deposition [15].

This project involves the growth and functionalisation of boron-doped C(110) single-crystal diamond (SCD) to produce thermally stable, low work function NEA surfaces. Two chemical vapour deposition (CVD) grown C(110) samples were analysed to assess growth reproducibility and determine the electronic properties of H-terminated C(110) compared to C(100). Surface chemistry was functionalised via controlled oxygen treatment, with a non-evaporable getter (NEG) pump installed, and compared against reported C(110) data obtained without a NEG, as well as C(100) results of Zulkharnay *et al.* [13]. Long-range surface order and roughness were assessed before and after a high-temperature anneal, and surface chemistry and electronic properties were analysed over three cycles of oxygen-lithium functionalisation.

Stable, low-work-function diamond surfaces have broader commercial applications, including long-lived betavoltaic nuclear batteries for deployment in remote environments such as space and undersea, gammavoltaic energy harvesting, and solar-powered TECs for off-grid electricity generation [4, 12, 17, 18]. The core aim of this project is to establish the relationship between termination chemistry and electronic properties for C(110) diamond, an important step towards understanding the reproducibility and effectiveness of the orientation for next-generation emission devices.

2 Background Theory

2.1 Work Function and NEA in Diamond

In a semiconductor, the valence band maximum (VBM) is the highest occupied state and the conduction band minimum (CBM) is the lowest unoccupied state, separated by a bandgap E_g. The Fermi level E_F is defined as the energy at which the occupation probability is 50% and, in an undoped semiconductor at low temperature, lies within the bandgap [3]. The vacuum level E_{vac} is defined as the energy of an electron at rest just outside the material surface [3]. The work function ϕ and electron affinity χ are then defined as,

$$\phi = E_{vac} - E_F, \tag{1}$$

$$\chi = E_{vac} - E_{CBM}, \tag{2}$$

where ϕ is the minimum energy required to remove an electron from the material, and χ represents the energy barrier facing conduction band electrons reaching the surface [3, 10]. The work function is not a fixed bulk property and depends on doping, crystallographic orientation, and surface adsorbates [3, 10]. Clean metallic cathodes such as W and Mo have ϕ values in the range $4-5\,\text{eV}$, whereas H-terminated samples can exhibit ϕ values near $3-4\,\text{eV}$ [2, 2, 19]. The positions of these energy levels for both PEA and NEA configurations are illustrated in Figure 1.

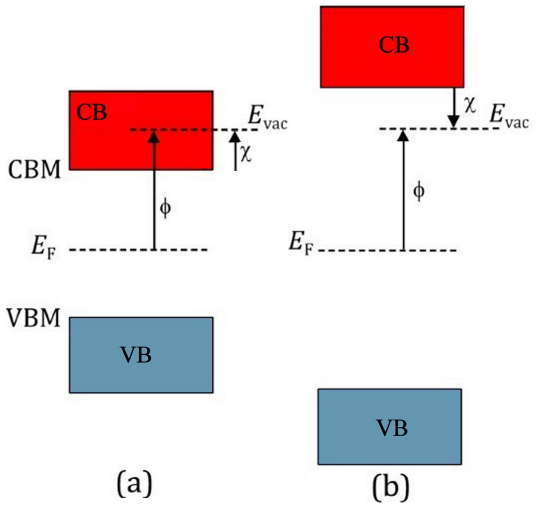

Figure 1. Illustration of the CBM, VBM, E_F, E_{vac}, work function (ϕ) and electron affinity (χ) for a) positive electron affinity (PEA) and b) negative electron affinity (NEA) configurations [20].

In most semiconductors E_{vac} lies above the CBM, giving PEA ($\chi > 0$), so conduction band electrons must overcome an energy barrier to reach vacuum. In NEA materials, surface dipoles shift E_{vac} below the CBM such that $\chi < 0$ and conduction band electrons can escape without any energy barrier [10, 20]. Diamond's ultra-wide band gap of $\sim 5.47\,\text{eV}$ positions the CBM well above typical Fermi levels, so a sufficiently strong surface dipole can shift E_{vac} below the CBM without disrupting bulk electronic structure, making NEA achievable through surface functionalisation [19, 21].

A distinction exists between 'true' and 'effective' NEA. In true NEA, E_{vac} lies below the CBM throughout the near-surface region. In effective NEA, E_{vac} the bulk retains PEA, but downward band bending at the surface locally pulls E_{CBM} above E_{vac} creating a region where electrons experience no barrier to emission [22]. These cases are illustrated schematically in Figure 2.

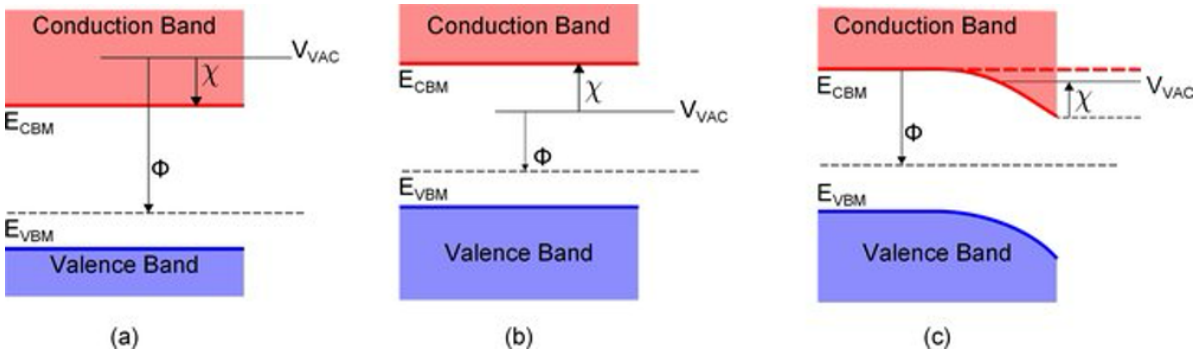

Figure 2. Illustration of (a) positive electron affinity (PEA), (b) 'true' negative electron affinity (NEA), (c) an 'effective' NEA [22].

The first experimental observation of true NEA on diamond was reported by Himpsel *et al.* on C(111) in 1979, with Van der Weide *et al.* demonstrating the same effect on C(100) in 1994 [23, 24]. H-terminated diamond has since become a standard NEA system, with values in the range -0.9 to $-1.0\,\text{eV}$ measured on C(100) and C(111) by Diederich *et al.* [25]. However, H-termination is limited by thermal instability above $\sim 700^o$C and by NEA loss under air exposure, driving the search for alternative surface treatments capable of maintaining NEA under conditions required for thermionic and vacuum-based devices [2, 7].

2.2 Boron Doped Diamond (BDD)

Undoped diamond has an extremely low carrier concentration at room temperature and negligible conductivity due to its wide band gap [13, 26]. During CVD growth, a boron atom (three valence electrons) substitutes for a carbon atom (four valence electrons) in the lattice, leaving one bond unsatisfied. This missing electron forms an acceptor level ∼0.39 eV above the VBM [27, 28]. Thermal or photon-induced ionisation of these acceptors promotes electrons to the acceptor level, leaving behind mobile holes in the VBM that act as a charge carriers for p-type conductivity. As boron concentration increases, E_F shifts closer to the VBM and resistivity falls, so the surface transitions from an insulator at low doping levels to a semiconductor materials with $\rho \sim 10^{-3}\Omega cm$ at boron concentrations approaching $10^{20} cm^{-3}$, as reported by Gong *et al.* in Figure 3 [29]. At high enough concentrations, BDD becomes a p-type semiconductor exhibiting metallic-like transport properties [27, 28].

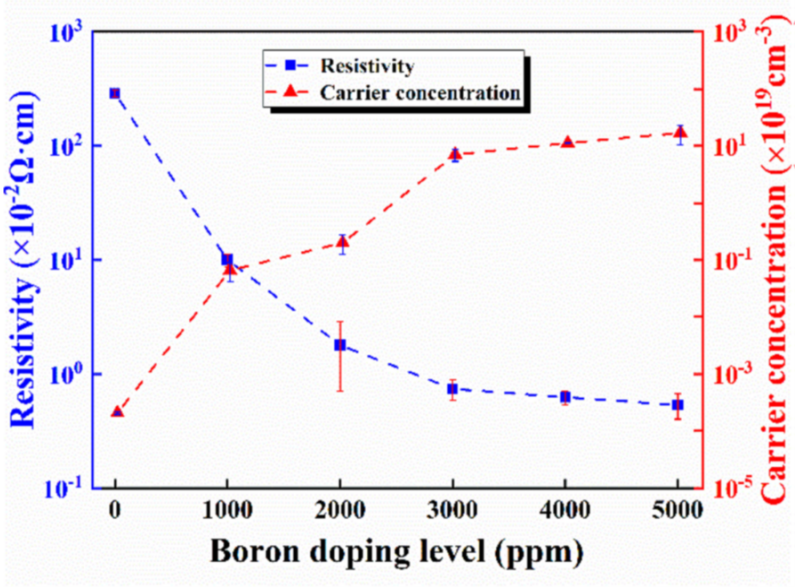

Figure 3. The relationship between carrier concentration and resistivity in BDD as a function of boron doping level, showing a decrease in resistivity and an increase in p-type conductivity with higher dopant concentrations [29].

Boron-doping serves two purposes in this project. First, it provides the bulk conductivity required for charge transport [29]. Second, it ensures electrical grounding during UHV photoemission measurements, as a sufficiently conductive surface suppresses charging effects that would otherwise distort photoemission spectra, enabling reliable determination of ϕ and χ [7, 13, 30].

2.3 Surface Functionalisation and Dipole Formation

Diamond surfaces contain reactive dangling bonds that are stabilised by the adsorption of terminating species, whether during growth or through active functionalisation. The nature of the terminating species determine the direction and magnitude of the resulting surface dipole, through charge redistribution driven by the electronegativity difference between carbon and the adsorbate [11]. This dipole shifts E_{vac} relative to the bulk electronic structure, changing ϕ and χ [2, 10, 13].

2.3.1 Hydrogen Termination

Hydrogen has a lower electronegativity than carbon, so C-H bonds produce a partial negative charge on carbon and a partial positive charge on hydrogen [10]. The resulting dipole is oriented with its positive end toward vacuum, lowering E_{vac} relative to the CBM and producing NEA, as shown in Figure 4 and 5 [2]. Maier *et al.* reported

values as negative as $\chi \sim -1.3eV$ on H-terminated C(100) [11]. H-terminated diamond is therefore widely used as a standard NEA system [31].

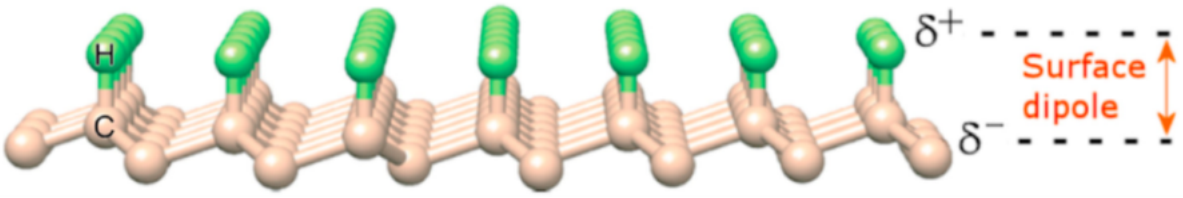

Figure 4. Illustration of the surface dipole formed by C–H bonds on H-terminated diamond, which implicitly gives rise to a downward shift of the vacuum level relative to the CBM and subsequent NEA [2].

However, hydrogen desorbs at temperatures above $\sim 700^oC$, eliminating the C-H dipole, and atmospheric exposure progressively replaces C–H bonds with hydroxyl groups (C–OH), whose opposing dipole orientation further suppresses NEA [7, 31]. This instability makes H-termination unsuitable for thermionic devices and vacuum devices, which require sustained emission at elevated temperatures or long-term air exposure [2, 12].

2.3.2 Metal-Oxygen Termination

Oxygen Treatment

A surface is treated with oxygen to provide atmospheric stability by reducing reactivity and degradation under air exposure, improving on the limitations of H-termination [13]. Oxygen is more electronegative than carbon, so when it bonds to the diamond surface, in groups such as ether bridges (C–O-C), ketone (C=O), and hydroxyl (C–OH), electron density is transferred from the carbon toward oxygen [10, 32]. The resulting dipole is oriented with its negative end at oxygen and its positive end toward the carbon bulk [10]. This raises E_{vac} above the CBM, as shown in Figure 5, producing PEA. Maier *et al.* measured $\chi = 1.7\,\text{eV}$ on oxidised C(100) diamond, with ϕ in the range $4 - 6\,\text{eV}$[11]. O-treated diamond surfaces therefore exhibit poor electron emission properties when applied alone [32].

The relative proportions of ether, ketone, and hydroxyl species present within oxygen layer depend on the oxidation method and conditions [13]. Zulkharnay *et al.* demonstrated that molecular (O_2) treatment of C(100) achieved ~6.47% oxygen coverage, or effective 90%, when the UV-ozone result of 7.49% is taken as full coverage [13].

Lithium Deposition and Combined O-Li Termination

Lithium has very low electronegativity and donates electron density when adsorbed onto O-treated diamond [33]. Lithium atoms bond preferentially to surface oxygen species, forming C–O–Li, Li_2O and Li-Li cluster environments, all identifiable in photon spectroscopy [13]. Charge transfer from lithium to oxygen produces a dipole with its positive end at lithium and its negative end centered partway along the underlying C-O bond, counteracting the O-treatment-induced dipole and lowering E_{vac}, as shown in Figure 5 [33].

At sufficient lithium coverage, this O-Li dipole restores NEA, as shown in Figure 5. Density functional theory (DFT) calculations by O'Donnell *et al.* predicted χ values as large as $-3.9\,\text{eV}$ for lithium on oxidised C(100), while recent experimental work by Zulkharnay *et al.* achieved an $\chi = -1.68\,\text{eV}$ using molecular O_2 treatment followed by lithium deposition [13, 31]. Increased O-Li bonding, demonstrated by the fractional growth of C–O–Li components in photon spectroscopy, correlates to a stronger dipole, reduced ϕ, and larger NEA [13].

The magnitude and direction of the surface dipole can therefore be controlled through the choice of terminating species and their electronegativity. This allows the control of diamond's electronic surface properties, with oxygen-lithium termination offering both large NEA and improved thermal and vacuum stability compared to H-termination.

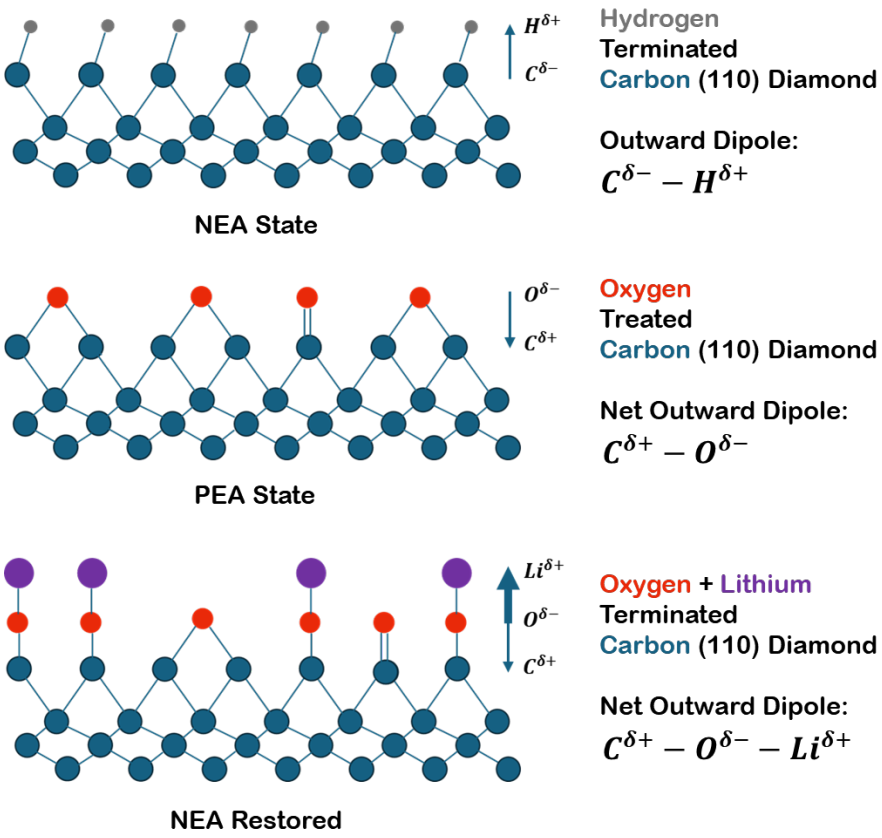

Figure 5. Author-generated illustration of the three central diamond surface terminations and their effect on dipole formation (generic bulk carbon structure used). Hydrogen termination produces a ($C\delta^-$–$H\delta^+$) dipole (grey bonds on blue carbon) that lowers the vacuum level, giving NEA. Oxygen treatment (red) forms ether, ketone, and hydroxyl (not shown) configurations, producing an opposing ($C\delta^+$–$O\delta^-$) dipole that raises the vacuum level and gives PEA. Lithium deposition (purple) onto the O-treated surface forms C–O–Li bonds with a $C\delta^+$–$O\delta^- - Li\delta^+$ dipole, restoring NEA at sufficient coverage with improved stability over H-termination.

2.4 Crystallographic Orientation and Surface Reconstruction

Miller indices (hkl) (e.g. (110)) define the orientation of atomic planes within a crystal lattice, as shown in Figure 6. Each orientation contains a different arrangement of surface atoms, with differing dangling bond densities and geometries [16, 22]. Diamond can be grown in polycrystalline or single-crystal form. Polycrystalline films contain grain boundaries and regions of varying orientation that introduce surface inhomogeneity and limit the reproducibility of NEA measurements, whereas SCD exposes a well-defined (hkl) surface, making it the preferred choice for diamond surface studies [34].

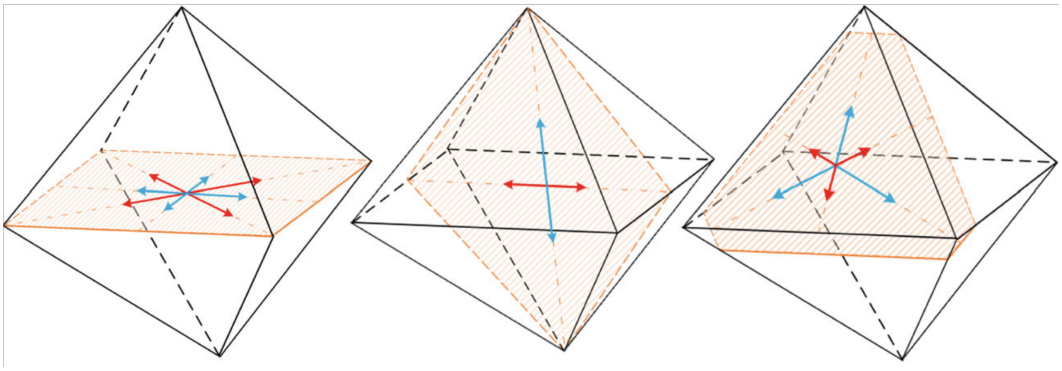

Figure 6. Illustration of a standard C(100) (square) plane, C(110) (rectangular) plane and C(111) (triangular) plane [35].

The unreconstructed C(100)-(1×1) surface presents two dangling bonds per carbon atom, while each top layer atom on C(111)-(1×1) has only one dangling bond perpendicular to the surface connected by three back-bonds [16]. C(110) similarly presents one dangling bond per surface atom, arranged in zigzag rows rather than hexagonal [16].

These unsaturated dangling bonds, which reappear after H-termination is desorbed at high temperature, are energetically unfavourable. The same annealing step supplies the thermal energy needed for surface atoms to rearrange into lower-energy configurations [14, 16]. Both C(100) and C(111) reconstructions are confirmed by (2×1) LEED patterns after annealing, forming C-C dimers and Pandey π-bonded chain reconstructions respectively [14, 16]. In contrast, C(110) does not reconstruct and simply relaxes within its 1×1 periodicity, forming π-bonded zigzag chains that partially saturate dangling bonds, as shown in Figure 7 [16].

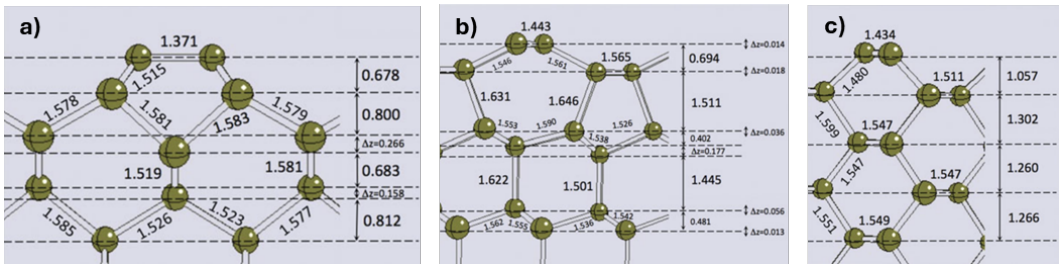

Figure 7. Surface structures for a) C(100)-(2×1) reconstruction b) C(111)-(2×1) reconstruction and c) C(110)-(1x1) relaxed unreconstructed surface [16].

The surface structures serve as templates for controlled functionalisation, as oxygen bonds to the available surface sites in ether bridge (C–O–C) or ketone (C=O) configurations, and subsequent lithium deposition forms the O–Li dipoles that induce NEA [13, 36]. The strength of oxygen bonding differs between orientations. Baumann and Nemanich showed that oxygen is most strongly bound on C(100), where each surface atom has two available bonds, requiring 900–1050^{o}C for complete removal, whereas on C(111) and C(110), each atom presents only one dangling bond, and oxygen is removed at 600–700^{o}C [14].

C(110) has received comparatively less attention, partly due to issues with its growth, preparation and the limited structural information available from its (1×1) LEED pattern, which make long-range surface order difficult to verify [15, 16].

3 Experimental Methods

3.1 MPCVD Growth of BBD

Boron-doped single-crystalline C(110) films were grown using microwave plasma chemical vapour deposition (MPCVD) in the University of Bristol Diamond Laboratory 'Back Reactor'. MPCVD is a well-established method for producing high-quality diamond thin films with precise control over growth rate, crystal size and surface morphology [37]. In MPCVD, microwave radiation energises gas to form a sphere of plasma above a heated substrate, which decomposes the input gas mixture into reactive species that deposit homoepitaxial single-crystal thin film layers [37].

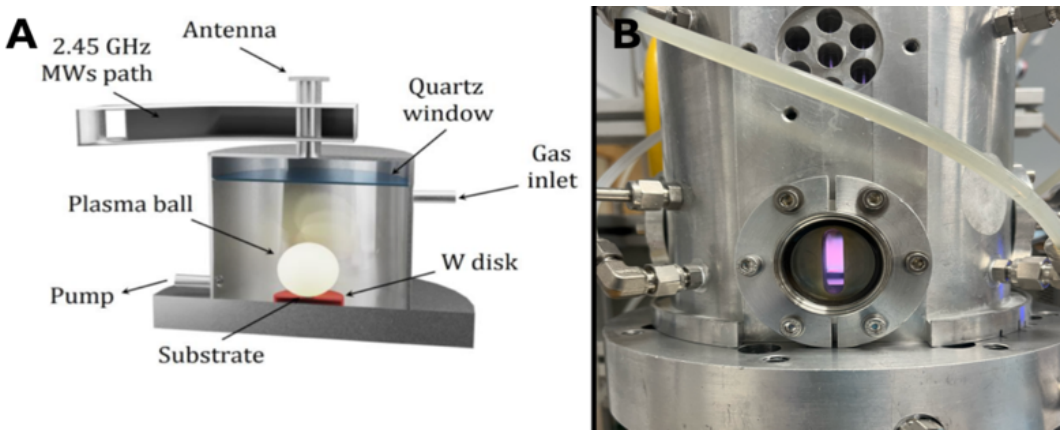

Figure 8. A) An illustration of the MPCVD showing the location of the substrate, the plasma ball, the gas inlet, vacuum pump and the quartz window at the top of the chamber and B) Exterior photograph of the MPCVD showing the glowing purple plasma [38].

Microwave irradiation dissociates molecular hydrogen (H_2) into atomic hydrogen, which stabilises sp^3 carbon bonding at the surface and promotes the formation of a diamond cubic lattice by etching non-diamond carbon, resulting in a H-terminated surface [39, 40]. Methane (CH_4) then provides the reactive carbon source for diamond layer formation [39].

P-type doping was achieved by introducing diborane (B_2H_6) into the H_2/CH_4 plasma. Under plasma conditions, diborane decomposes and boron atoms substitute into the growing lattice, forming acceptor levels 0.39 eV above the VBM [39, 41, 42]. Growth parameters included volumetric gas flow rates of 300 sccm (standard cubic centimetres per minute) for H_2, 12.5 sccm for CH_4, and 0.5 sccm for B_2H_6, with substrate temperatures maintained at 800-900^{o}C. For the initial hydrogen plasma-forming strike, chamber pressure was set to 15 Torr at a power of 0.6 kW, later increased to 60-120 Torr at 1.2 kW for CH_4 and B_2H_6 incorporation. Growth time was set to 1 hour. These conditions were chosen to target a boron concentration of 10^{20}cm^{-3}, similar to Gong *et al.*, yielding resistivities of $10^{-3}\Omega$cm, sufficient for adequate surface conductivity and reliable photoemission analysis without charging effects [7, 13, 29, 30]

A consequence of the hydrogen-rich plasma is the automatic H-termination of the surface during growth [12]. While not the target functionalisation, this termination acts as a starting point for characterisation. It degrades under atmospheric conditions over several days and required re-termination before transfer to the NanoESCA for UHV photoemission measurements.

3.2 NanoESCA UHV Surface Preparation

All surface preparation, including annealing, oxygen treatment, and lithium deposition was carried out in the NanoESCA system at the University of Bristol under UHV conditions. UHV is essential for producing well-defined surfaces, by minimising exposure to residual water vapour and hydrocarbons, which alter surface bonding, increase

ϕ, and suppress NEA.

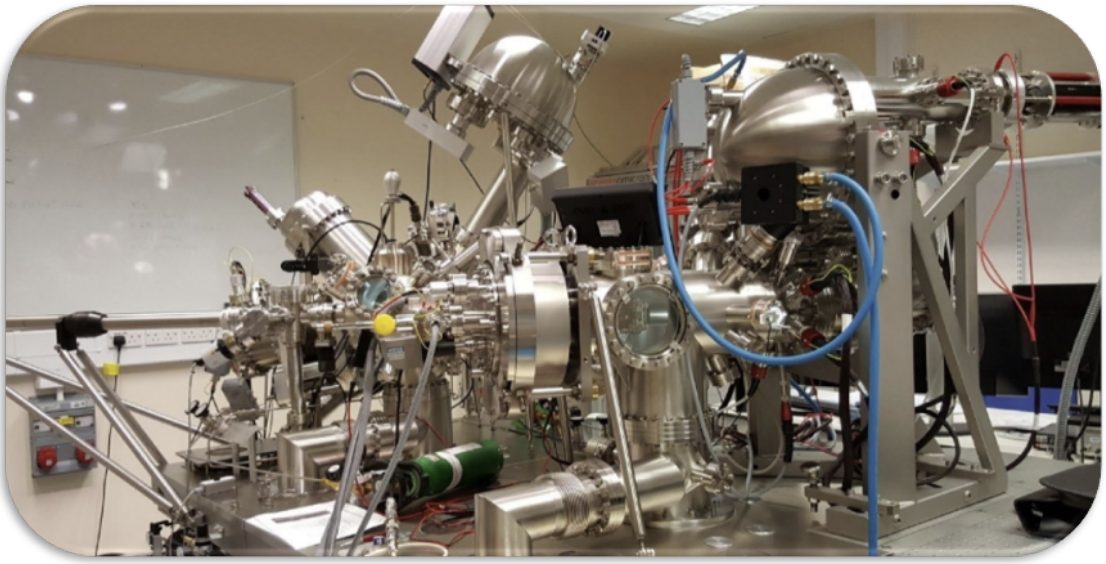

Figure 9. A photograph of the NanoESCA laboratory [43].

3.2.1 Annealing

Thermal annealing under UHV was used to desorb contaminants accumulated during transfer from the MPCVD and adsorbed from outgassing chamber walls during photoemission analyses. Annealing was performed by resistive heating of a coiled tungsten filament placed behind the molybdenum sample holder, with the current increased incrementally to the target value while the chamber pressure was maintained below 1.05×10^{-7} mbar to prevent readsorption of outgassed species [7]. Three annealing temperatures were applied at different stages of the workflow.

300^oC Anneal

A 300°C anneal, achieved at a filament current of 2.26A for ∼1 hour, was used to remove weakly bound adsorbates such as water vapour, upon entering the UHV system and prior to H-terminated surface analysis and NEG installation [7, 13]. This temperature is insufficient to break C–H bonds, so H-termination was preserved.

500^oC Activation Anneal

A 500°C anneal, achieved at 3.80A for 45 minutes, served as the activation anneal between oxygen treatment and lithium deposition cycles. At this temperature, lithium atoms acquire sufficient energy to rearrange into stable C-O-Li bonding configurations, driving structural reorganisation of the surface layer toward a favourable NEA state [44].

900^oC High-Temperature Anneal

A 900°C anneal, achieved at 7.00A, was used once to desorb H-termination and expose the underlying bare C(110) surface, in preparation for the first oxygen treatment and lithium deposition cycle [7, 8]. This anneal also enabled LEED characterisation, as H-termination disrupts the long-range order of the surface and its removal allows the C(110)-(1×1) periodicity to be observed. LEED measurements were taken before and after this anneal to verify the surface structure and to confirm hydrogen desorption through intensity, sharpness and reduced background of the diffraction spots [7, 10, 45, 46, 47].

3.2.2 Non-Evaporable Getter (NEG) Pump

A NEG pump was installed in the NanoESCA to improve UHV quality during surface functionalisation. NEG pumps consist of a reactive getter material, typically based on zirconium or titanium alloys, that chemisorbs active gas molecules, including H_2, H_2O, CO, CO_2, and N_2 [48]. In the case of hydrogen, H_2 dissociates on the getter surface and the resulting atoms diffuse into the bulk of the getter material, giving NEG pumps a particularly high sorption capacity for H_2 [48]. The purpose of the NEG in this work was to remove residual water vapour outgassed from the metallic chamber during and after the 900^oC anneal, which would otherwise adsorb onto the bare diamond surface and form C-OH groups. Any adsorption would reduce effective oxygen by occupyinng bonding sites prior to O-treatment, in turn limiting the density of C–O–Li bonds formed during lithium deposition.

3.2.3 Surface Functionalisation Procedure

Surface functionalisation was carried out in the Front-End Loader (FEL) chamber of the NanoESCA, which provided the controlled UHV environment required for oxygen treatment and lithium deposition.

Molecular Oxygen (O_2) Treatment

Controlled molecular O_2 exposure was used to provide oxygen bonding sites prior to lithium deposition. Oxygen bonds to the surface in a mixture of ether (C–O–C), ketone (C=O), and hydroxyl (C–OH) configurations, with the proportion of each depending on oxidation conditions [13, 32]. XPS analysis after O-treatment determines the pre-lithiation oxygen coverage and the dsitribution of oxygen groups available for lithium bonding [13, 32]. Oxygen treatment was achieved through the controlled release of molecular O_2 from a gas canister into the FEL chamber, at a pressure of 1×10^{-2} mbar for 5 minutes.

Lithium Deposition and O-Li Cycles

Lithium was deposited onto the O-treated diamond by thermal evaporation of a heated solid lithium source within under UHV. Lithium bonds to surface oxygen species, forming C–O–Li bonds that produce a strong surface dipole counteracting oxygen-induced PEA [13]. With each successive oxygen–lithium cycle, the C–O–Li bond and associated surface dipole are expected to strengthen, progressively lowering ϕ and increasing NEA [13]. A target coverage of $\sim 2/3$ monolayer (ML) of lithium was deposited per cycle, corresponding to 2 lithium atoms per 3 carbon atoms. This was achieved by operating the lithium evaporator at 485^oC (2.85A filament current) for 203 seconds, and a 500^oC activation anneal followed each deposition to drive the O-Li termination toward a favourable NEA state [44]. The chamber pressure was expected to rise with each cycle, consistent with the accumulation and release of surface-bound species during activation annealing.. After each step, core-level XPS spectra (C 1s, O 1s, Li 1s) were produced to track the evolution of O-Li bonding [13].

3.3 NanoESCA UHV Surface Analysis

Surface analysis was performed using the NanoESCA system under UHV. The system integrates XPS, EF-PEEM, UPS and SPA-LEED within connected chambers, enabling chemical and electronic characterisation without breaking vacuum [13]. On the first measurement session for each technique, the analysis position was aligned so that all subsequent photoemission measurements were performed at roughly the same location on the surface.

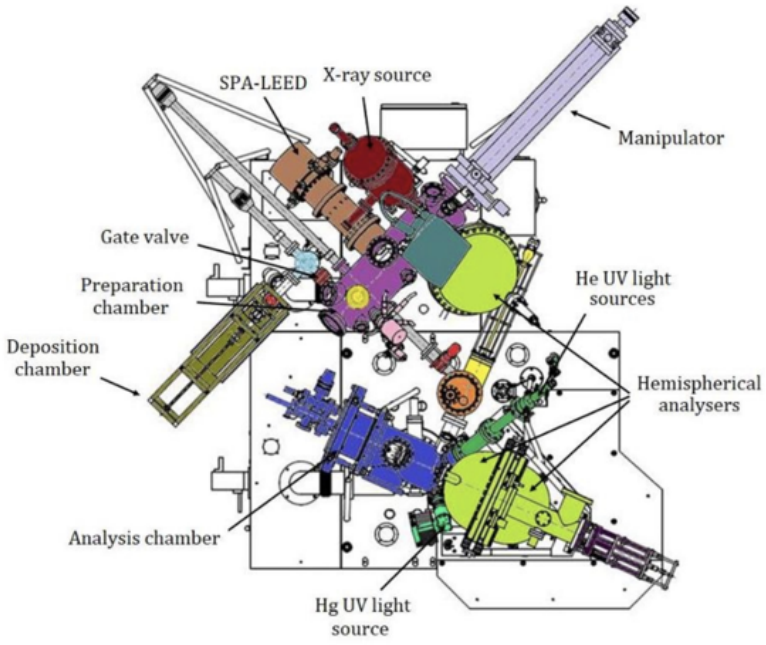

Figure 10. A top-down visual of the NanoESCA system showing the manipulator used to move samples to different analysis positions in the preparation chamber. The X-ray source (for XPS) and SPA-LEED located in the preparation chamber. The deposition chamber where oxygen treatment and lithium deposition occurs and the mercury or helium UV sources used for EF-PEEM and UPS within the analysis chamber [38].

3.3.1 X-Ray Photoelectron Spectroscopy (XPS)

XPS operates using the photoelectric effect, where incident monochromatic X-rays from an $AlK\alpha$ source ($h\nu =$ 1486.6eV) excite core level electrons, producing photoemission from the near-surface region [22]. The key energy relationship is,

$$h\nu = E_b + E_k + \phi, \tag{3}$$

where E_k is the emitted photoelectron kinetic energy, E_b represents binding energy, and ϕ here represents the $4 - 5\,\text{eV}$ analyser work function, which is corrected for during scanning. Core-level E_b values identify surface components, while chemical shifts in E_b reflect changes in local bonding environment [49]. Emitted electrons are energy-analysed in a concentric hemispherical analyser that passes only electrons within a selected range to the detector [49]. Because inelastic scattering limits the escape depth, $\sim$95% of the detected signal originates from the outermost $\leq$10nm, making XPS highly surface-sensitive [49].

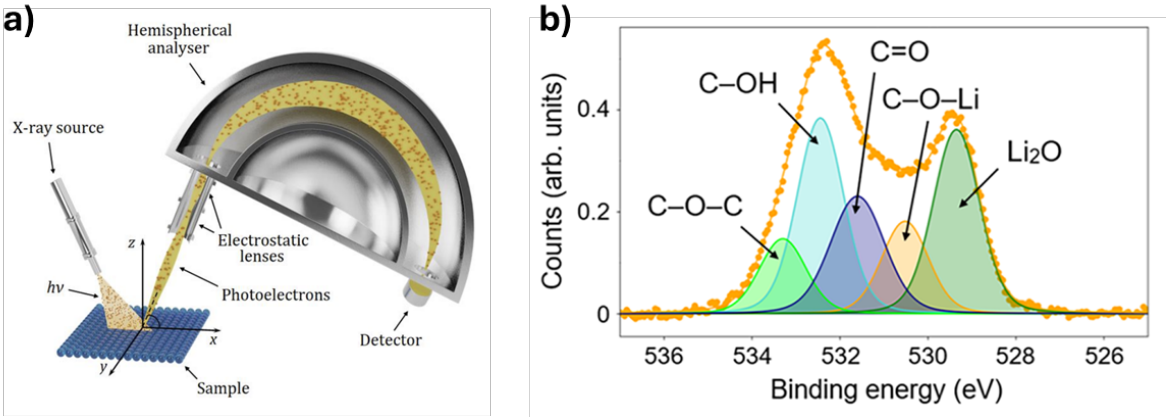

Figure 11. a) Diagram of the XPS apparatus and b) an example XPS spectrum for molecular O_2 treated and lithiated C(100) from Zulkharnay *et al.* showing a well-fitted O 1s spectrum [13, 38].

For O-treated diamond, distinct C–O–C, C=O, and C–OH configurations can be fitted within the O 1s spectrum, and their relative abundances analysed across functionalisation cycles [12]. This project focuses on the C 1s, O 1s, and Li 1s spectra to monitor surface carbon chemistry, oxygen groups, and lithium species introduced during deposition [13].

Spectra were fitted in CasaXPS using a constrained model with fixed inter-species E_b gaps for oxygenated and lithiated diamond surfaces determined by Zulkharnay *et al.* [13]. The C 1s envelope was fitted into sp^3 C–C (bulk and surface), C–O and C=O components. The O 1s region was modelled with C–O–C, C–OH, and C=O components, with additional C–O–Li and Li_2O contributions included after lithiation, as supported by Figure 11b. The Li 1s region was fitted with a two-component model including metallic cluster-like Li–Li and a oxygen-bonded (C–O–Li/Li_2O) components [13]. Shirley backgrounds were applied for C 1s and O 1s, while a linear background was used for Li 1s. All components were fitted with a consistent Gaussian–Lorentzian line shape [49]. Component concentrations were interpreted from integrated peak areas and relative area percentages [13].

3.3.2 Energy-Filtered Photoemission Electron Microscopy (EF-PEEM)

EF-PEEM is a surface-sensitive imaging technique performed alongside region-selected UPS in the NanoESCA, providing micron-level spatial resolution of photoelectron emission [2, 13]. UV illumination from a He I source (21.22eV) excites photoelectrons, which are extracted by a 12 kV bias (at 4.2 A) applied between the sample and the extractor electrode [2]. The emitted electrons are energy-filtered through an imaging double-hemisphere analyser, and images are acquired at successive energies to produce maps of local ϕ across the surface, computed in MATLAB, as shown in Figure 12 [2, 13].

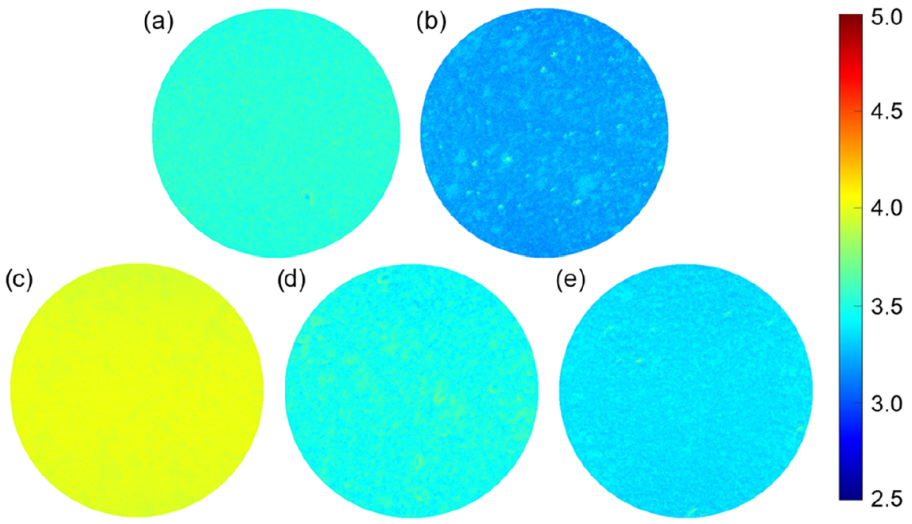

Figure 12. EF-PEEM work function maps from Zulkharnay *et al.* for lithiated C(100) diamond prepared by (a) UV-ozone and (b) molecular oxygen oxidation, after 64 hour atmospheric exposure (c, d), and following reactivation (e). Colour scale indicates local ϕ in eV and field of view is 37.5 μm [13].

In energy-filtered measurements, colour contrast is sensitive to the local ϕ, as regions with lower ϕ emit with less energy and appear at the low-ϕ end of the colour scale [13]. Surface-averaged ϕ values were extracted by generating pixel-resolved work function histograms over the field of view (typically tens of micrometres) and computing the mean and standard deviation in Python [13]. For polycrystalline samples, Andrade *et al.* observed pixel-to-pixel variations of up to 400 meV, providing a measure of surface uniformity [50]. On single-crystal surfaces, narrower distributions are expected, and apparent outliers should be interpreted as regions of insufficient termination coverage [2].

3.3.3 Ultraviolet Photoelectron Spectroscopy (UPS)

UPS probes the valence band electronic structure using UV excitation alongside EF-PEEM in the NanoESCA [2]. Because UV-excited photoelectrons have shorter inelastic mean free paths, UPS has nanometre-scale information depth and greater surface sensitivity than XPS, making it well suited for detecting changes in ϕ and NEA across functionalisation cycles [13].

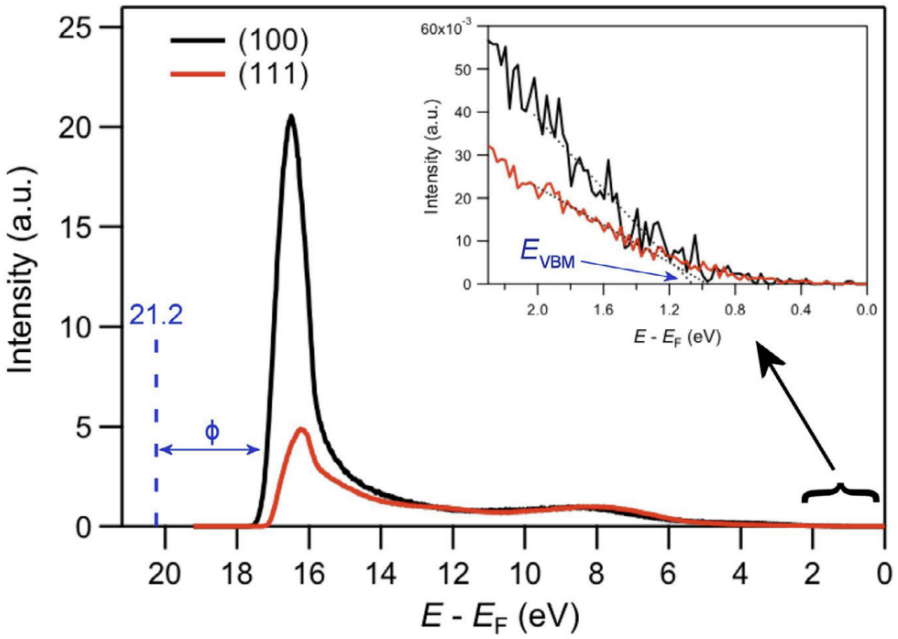

Figure 13. Example UPS spectra from James *et al.* for C(100) and C(111) diamond. The work function ϕ is the energy separation between $h\nu$ and the secondary electron cutoff E_{SECO}, while the VBM position E_{VBM} is located by valence band-edge extrapolation [2].

ϕ is calculated from the secondary electron cutoff (E_{SECO}) by extrapolating the low-kinetic energy reduction to zero intensity [51]. While reliable in principle, the uncertainty in SECO-derived ϕ values is increased by the extrapolation, particularly where spectral gradients are shallow. EF-PEEM-derived ϕ carries much smaller uncertainty and is therefore preferred for ϕ determination [13]. The relevant relationships are,

$$\phi = h\nu - E_{\mathrm{SECO}} \tag{4}$$

$$\xi = E_{\mathrm{VBM}} - E_F \tag{5}$$

$$\chi = \phi + \xi - E_g, \tag{6}$$

where $h\nu$ is the photon energy (21.22 eV for He I), E_{SECO} is the secondary electron cutoff, and ξ is the Fermi level to VBM separation [13, 51]. In UPS, E_F is corrected to 0 eV, so ξ equates to the measured E_{VBM} position, determined from the valence band-edge extrapolation shown in Figure 13. Using ϕ from EF-PEEM and ξ from UPS, χ is calculated via Equation 6 with $E_g = 5.47$ eV [13].

3.3.4 Spot Profile Analysis Low-Energy Electron Diffraction (SPA-LEED)

SPA-LEED was used to assess the long-range order and the surface smoothness of the C(110) samples before and after the 900°C anneal, confirming hydrogen desorption without a loss of surface order prior to oxygen treatment [7, 14].

In SPA-LEED, low-energy electrons are directed at the surface and the resulting diffraction pattern is scanned through electrostatic deflection relative to a fixed detector, enabling measurement of spot positions, widths, and background levels in reciprocal k-space, as shown in Figure 14 [7, 46]. Sharp, high-intensity spots on a low diffuse background indicate long-range order and limited defects, whereas spot broadening or increased background imply reduced order, higher defect densities and increased surface roughness [10, 13, 45, 46, 47]. Prior to each diffraction measurement, SEM-mode real-space scans were used to locate the most appropriate analysis region on the surface.

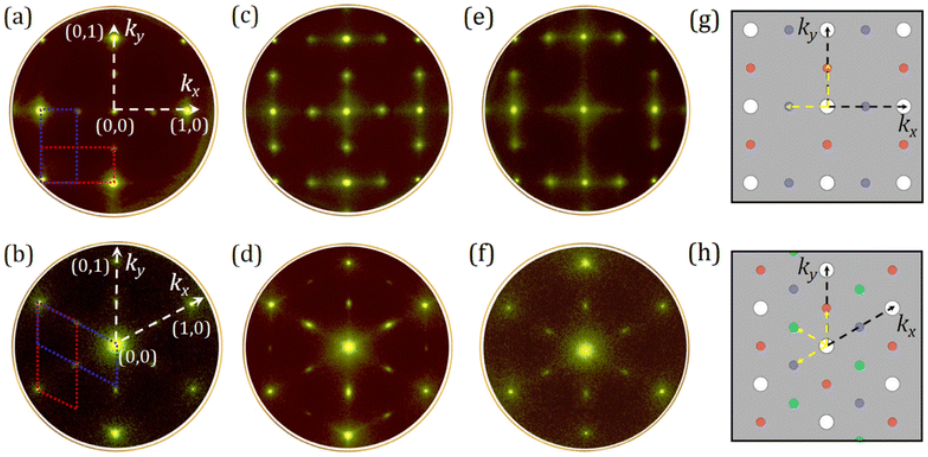

Figure 14. Example SPA-LEED patterns from Zulkharnay and May for bare and scandium-terminated C(100) and C(111) diamond at various preparation stages, collected at 100 eV and 150 eV respectively. The C(100) and C(111) surfaces exhibit four-fold and three-fold symmetries from two and three rotational (2×1) diffraction domains, respectively. Simulated reciprocal-space patterns are shown in (g) and (h) [7].

Two incident electron energy were used for each measurement. A lower-energy scan (∼92-96eV) provided greater sensitivity to the outermost atomic layers and typically yields higher spot intensities, while a higher-energy scan (∼144-148eV) improved spot sharpness through increased probe depth and reduced inelastic scattering [46, 14].

As discussed in Section 2.4, C(110) does not undergo a (2×1) reconstruction but relaxes to form π-bonded zigzag chains, typically retaining a (1×1) LEED pattern [14, 16]. Because the lack of reconstruction limits the structural information available from LEED on C(110), spot-profile analysis was not expected to be feasible. The SPA-LEED results for C(110) therefore serve as a qualitative indicator before and after annealing, assessing whether the 900 ^{o}C treatment improved surface order and smoothness, thereby confirming hydrogen desorption.

4 Results and Discussion

4.1 Sample Overview, Experimental Workflow and Reference Table for XPS Fitting

Three C(110) BDD samples were prepared for this study. Their orientation and respective roles are summarised in Table 1.

Sample	Orientation	Role in Project
BS1	C(110)	The central sample of this study, on which the full experimental workflow was performed, including surface cleaning, oxygen-lithium functionalisation cycles, and XPS, PEEM, UPS and SPA-LEED analyses.
BS2	C(110)	Damaged during a EF-PEEM discharge event and excluded from further analysis.
BS3	C(110)	Subjected only to initial characterisation steps (annealing, XPS, EF-PEEM, UPS) and used as a comparative H-terminated surface to assess reproducibility against BS1.

Table 1. Summary of samples investigated, their crystallographic orientation, and role within the project.

The experimental workflow applied to BS1 and BS3 is shown in Figure 15.

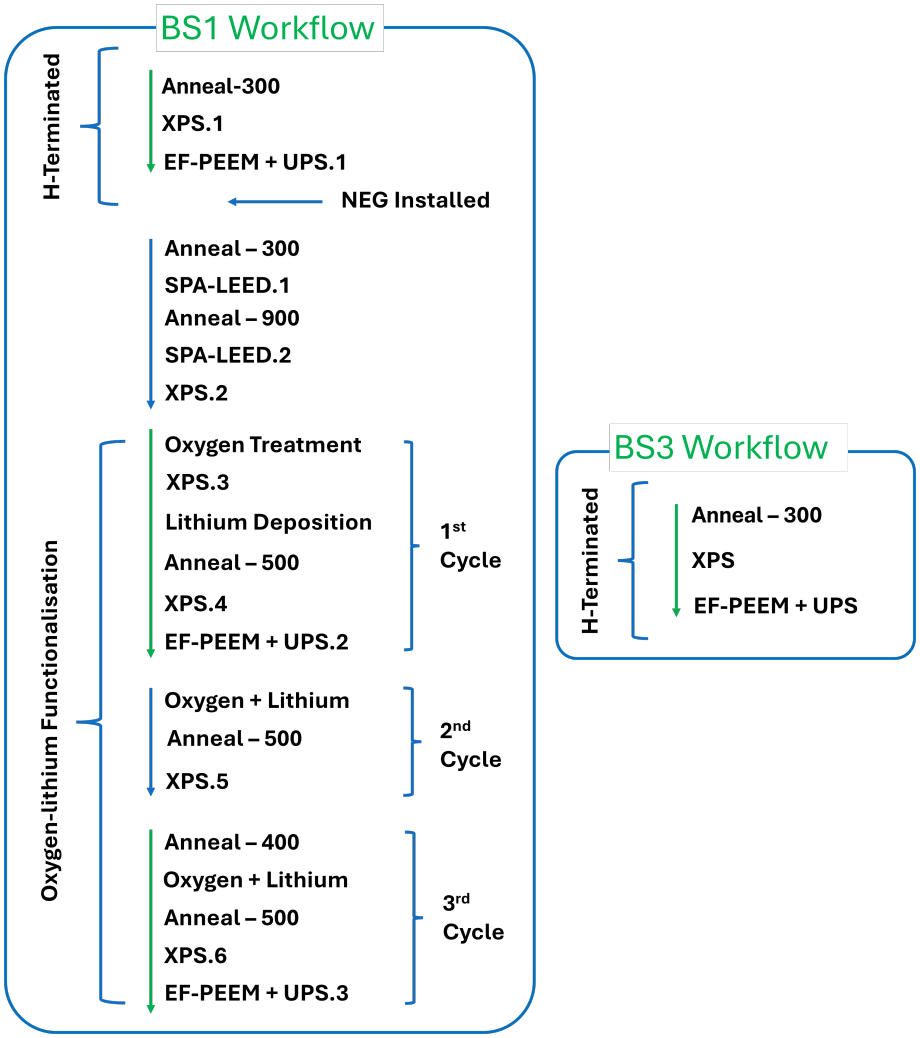

Figure 15. Flow diagram of the experimental workflow for BS1 (left) and BS3 (right) C(110) samples in chronological order.

Interpretation of the XPS spectra throughout this chapter relies on peak assignments established for lithiated C(100) surfaces. Table 2 reproduces the fitting results of Zulkharnay *et al.* for a molecular O_2 C(100) surface before and after lithium deposition, and is referred to throughout as the basis for inter-species binding energy gap assignments and component identification on the C(110) surfaces studied [13].

Element Spectrum	Surface Component	MoLO SCD(100)	
		BE (eV)	Rel. (%)
C 1s			
Pre-lithiation	sp^3 C–C (B)	284.43	86.4
	sp^3 C–C (S)	285.03	10.3
	C–O	285.83	2.2
	C=O	287.23	1.1
Lithiated	sp^3 C–C (B)	284.43	82.8
	sp^3 C–C (S)	285.08	14.6
	C–O	285.88	2.1
	C=O	287.28	0.5
O 1s			
Pre-lithiation	C–O–C	533.84	2.9
	C–OH	532.31	73.3
	C=O	531.63	23.9
Lithiated	C–O–C	533.30	11.0
	C–OH	532.45	28.6
	C=O	531.60	19.9
	C–O–Li	530.52	13.6
Li 1s			
Lithiated	Li^0 (Li–Li)	54.5	32.1
	C–O–Li (Li_2O)	55.79	67.9

Table 2. XPS results table for molecular O_2 C(100) surfaces before and after lithium treatment, as produced by Zulkharnay *et al.*, showing various element spectra prior to and after lithium deposition, the expected surface components, associated binding energies and relative percentage area of each component [13].

4.2 Reproducibility and Electronic Properties of Hydrogen-Terminated C(110) Diamond

Following MPCVD growth, BS1 and BS3 were transferred to the NanoESCA system and underwent the initial stages of the workflow shown in Figure 15. This included loading into UHV, a 300^{o}C anneal to desorb contaminants without removing C-H bonds, followed by XPS, EF-PEEM, and UPS analysis [7]. No oxygen or lithium functionalisation was performed at this stage, so measurements discussed below correspond to the H-terminated state.

This section addresses two questions. First, whether the surface chemistry and electronic structure of C(110) are reproducible between identical samples, tested by direct comparison of BS1 and BS3. Second, how do the H-terminated C(110) surface chemistry, ϕ, and χ compare with literature values reported by Diederich *et al.* for H-terminated C(100) and C(111).

4.2.1 Surface Chemistry: C 1s and O 1s Spectra

The C 1s and O 1s spectra for both samples are presented in Figure 16 and 17, with fitted components and relative areas summarised in Table 3. Peak assignments follow the reference fits of Zulkharnay *et al.* in Table 2 [13].

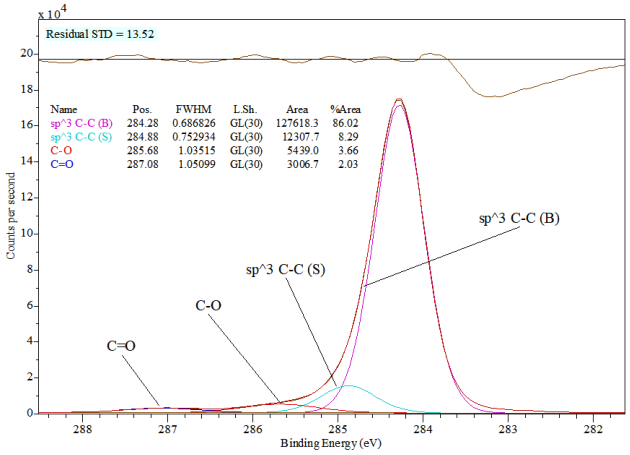

a) BS1 XPS.1 C 1s spectra

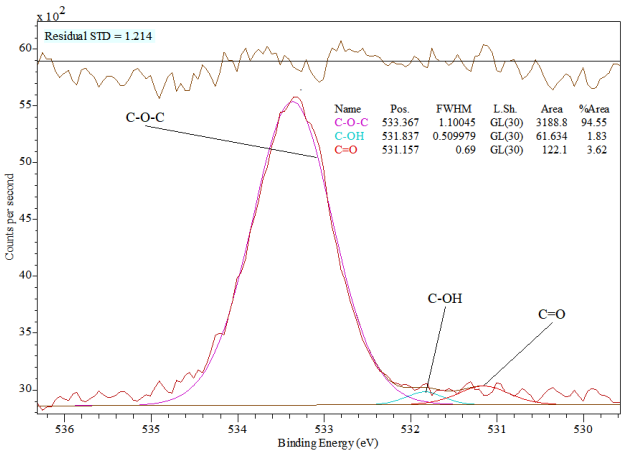

b) BS1 XPS.1 O 1s spectra

Figure 16. BS1 H-terminated C 1s and O 1s spectra

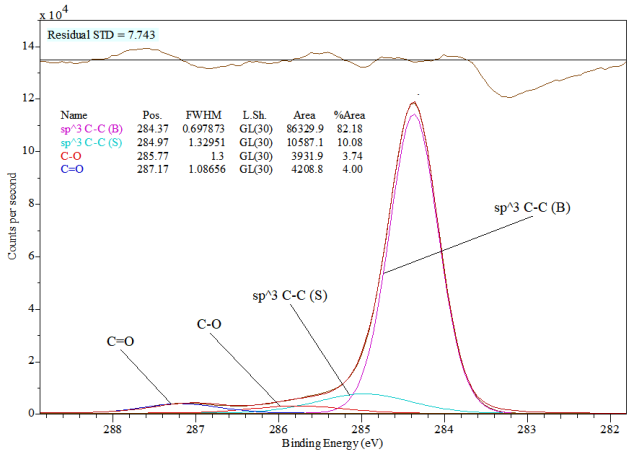

c) BS3 XPS C 1s spectra

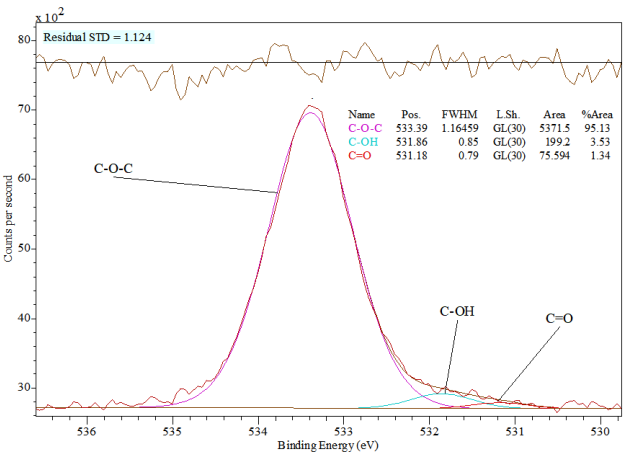

d) BS3 XPS O 1s spectra

Figure 17. BS3 H-terminated C 1s and O 1s spectra

Element Spectrum	Surface Component	BS1		BS3	
		BE (eV)	Rel. (%)	BE (eV)	Rel. (%)
C 1s					
H-terminated	sp^3 C–C (B)	284.28	86.02	284.37	82.18
	sp^3 C–C (S)	284.88	8.29	284.97	10.08
	C–O	285.68	3.66	285.77	3.74
	C=O	287.08	2.03	287.17	4.00
O 1s					
H-terminated	C–O–C	533.37	94.55	533.39	95.13
	C–OH	531.84	1.83	531.86	3.53
	C=O	531.16	3.62	531.18	1.34

Table 3. XPS fitting results for H-terminated BDD C(110) surfaces for BS1 and BS3, showing the expected surface components, binding energies, and relative peak areas percentages.

Reproducibility between BS1 and BS3

The C 1s spectra of both samples were dominated by the sp^3 bulk C-C component (86.0% for BS1 and 82.2% for BS3), with the sp^3 surface C-C contribution adding a further 8.3% and 10.1% respectively. Within the estimated

±1% fit uncertainty, the total sp^3 fractions (94.3% and 92.3%) agree to within ∼2%. The O 1s spectra were similarly consistent, with the C-O-C (ether) component accounting for over 94% of the oxygen signal in both samples. Binding energies for all fitted components match to within 0.1 eV, at the accepted level of calibration uncertainty [13].

The notable discrepancies above the ±1% fit uncertainty were the C=O contribution in the C 1s spectra, nearly double in BS3 (4.0%) compared to BS1 (2.0%), together with the increase in C-OH (1.8% to 3.5%) and reduction in C=O (3.62% to 1.34%). These differences are most likely due to longer air exposure and subsequent C-OH adsorption between growth and loading for BS3, or minor variations in the effectiveness of the 300°C anneal [7, 52]. With only two samples available, this observation establishes consistency between measurements rather than statistical reproducibility.

4.2.2 Electronic Structure of Hydrogen-Terminated C(110)

Having established in Section 4.2.1 that BS1 and BS3 were consistent in surface chemistry, the corresponding electronic properties were studied by EF-PEEM and UPS on the same surfaces.

The work function maps and histograms for BS1 and BS3 are shown in Figure 18 and 19, with the corresponding UPS spectra in Figures 20 and 21. Parameters calculated using Equation 5, 6, 7 are summarised in Table 7.

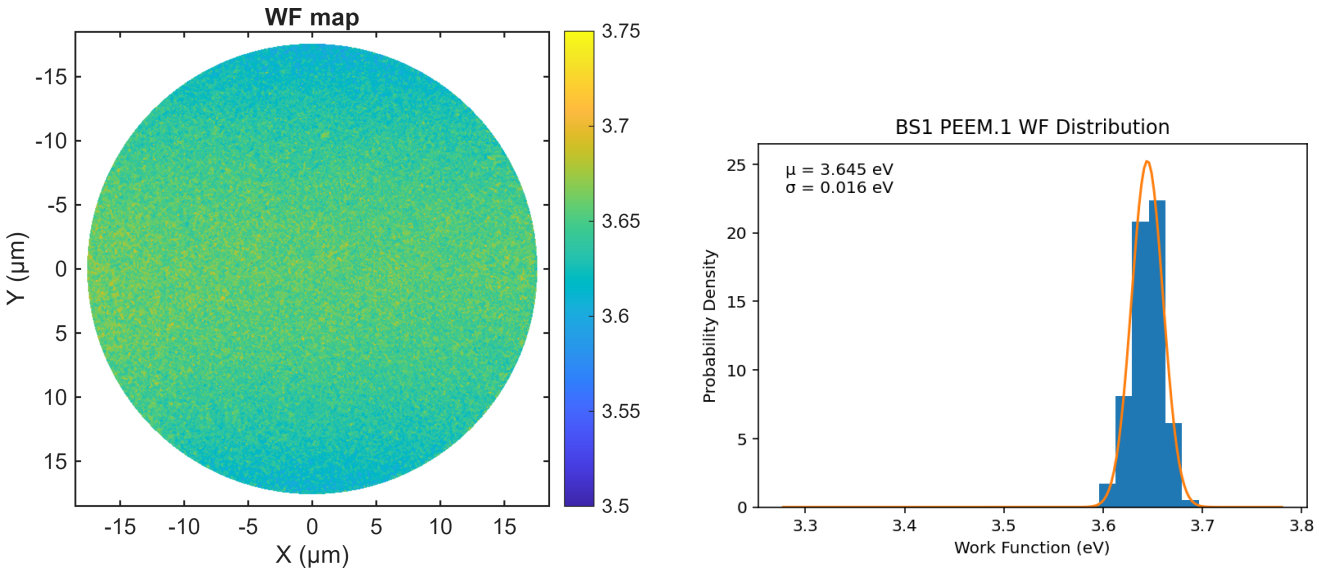

a) BS1 EF-PEEM.1 work function variation map

b) BS1 EF-PEEM.1 work function distribution histogram

Figure 18. BS1 hydrogen-terminated work function variation map and distribution histogram.

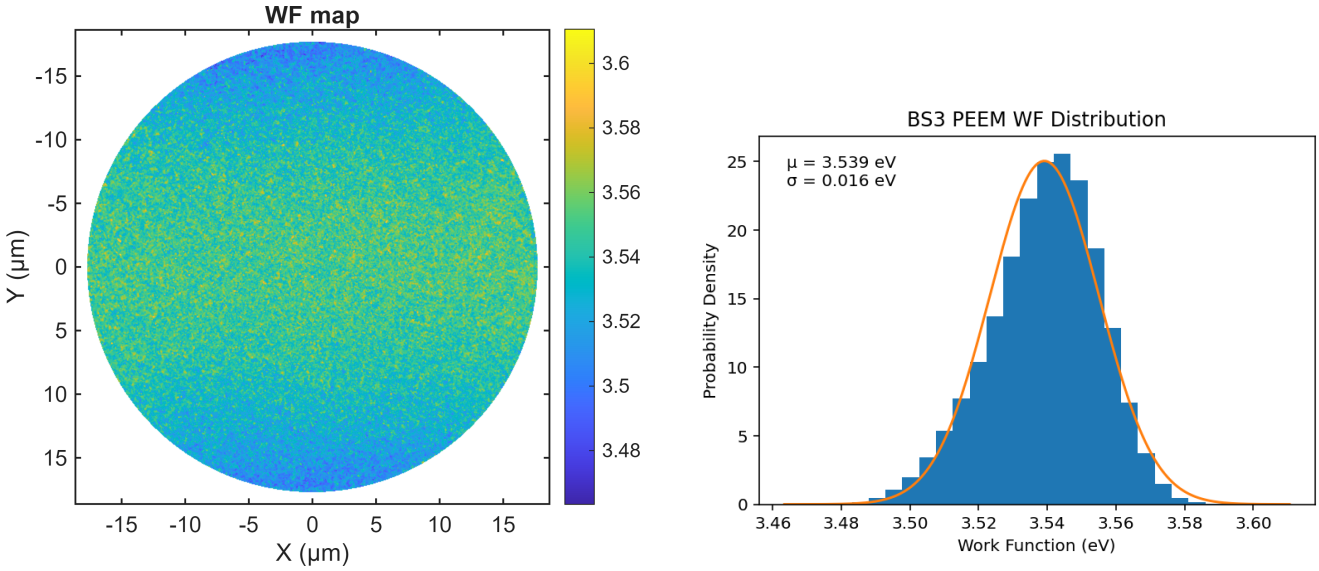

a) BS3 EF-PEEM work function variation map

b) BS3 EF-PEEM work function distribution histogram

Figure 19. BS3 hydrogen-terminated work function variation map and distribution histogram.

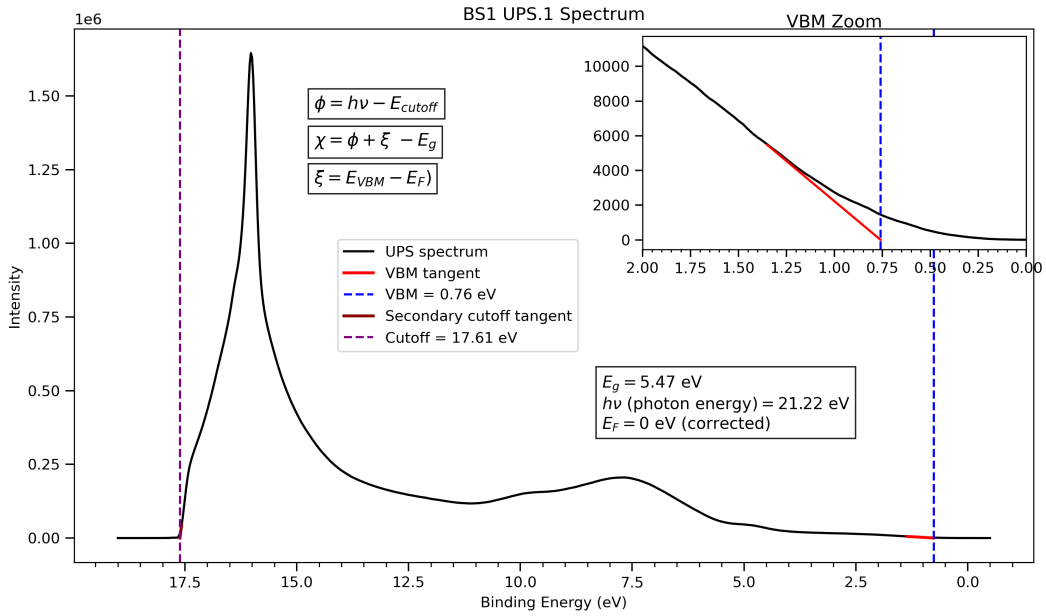

Figure 20. BS1 corresponding UPS.1 spectra to Figure 18 EF-PEEM results.

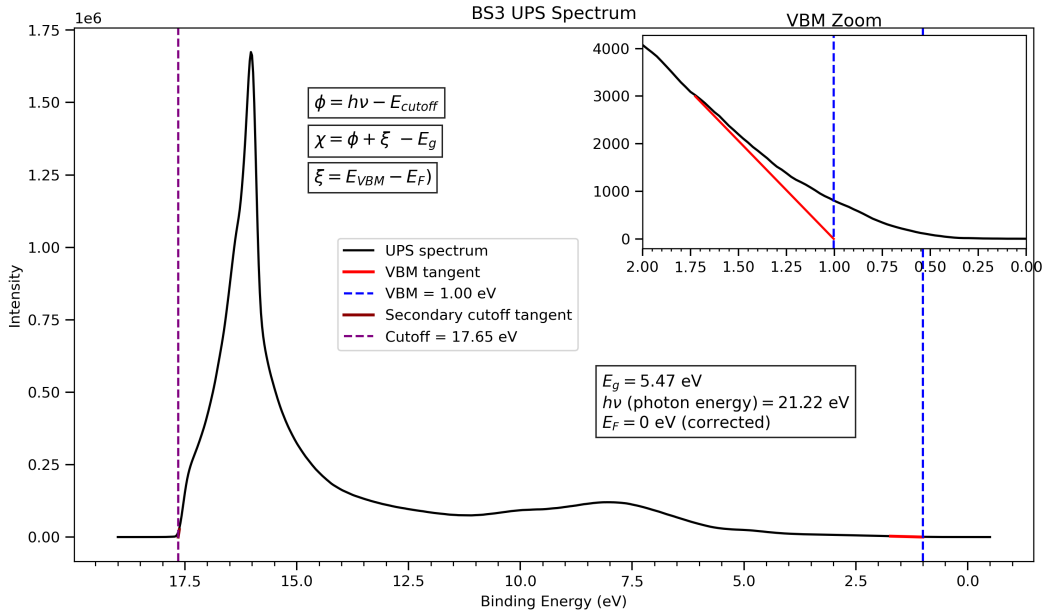

Figure 21. BS3 corresponding UPS spectra to Figure 19 EF-PEEM results.

Technique	Parameter	Sample	
		BS1	BS3
EF-PEEM	Mean ϕ	3.64	3.54
	Standard Deviation, σ	0.02	0.02
UPS	E_{SECO}	17.61	17.65
	E_{VBM}	0.76	1.00
	ϕ	3.61	3.57
	χ	-1.07	-0.93

Table 4. Summary of EF-PEEM and UPS results for H-terminated BS1 and BS3 samples, showing the two different techniques and there associated parameters.

Reproducability Between BS1 and BS3

The mean EF-PEEM work functions were 3.64 eV for BS1 and 3.54 eV for BS3, a difference of 0.10 eV reproduced almost exactly in the UPS-derived values (3.61 eV and 3.57 eV). The corresponding χ values were -1.07 eV and -0.93 eV, differing by 0.14 eV. BS3 had the lower ϕ of the two yet also the lower NEA, a result of its higher E_{VBM} (1.00 eV for BS3 compared to 0.76 eV for BS1), demonstrating a 0.24 eV upward shift of the valence band-edge relative to the Fermi level. Since $\chi = \phi + E_{VBM} - E_g$, this upward E_{VBM} shift outweighed the small downward shift in ϕ, which may indicate stronger downward band bending or a small difference in bulk doping between the two samples.

The work function distributions for both samples showed $\sigma = 0.02$ eV, identical to two decimal places. The local vacuum level therefore varied by less than 1% of its mean value across the $15 \times 15\mu$m field of view on both samples. These narrow distributions suggest that the H-termination was spatially uniform and the surface dipole density was roughly constant, consistent with the absence of grain boundaries, or contamination patches that produced the 0.4 meV variations observed on polycrystalline samples [50].

Comparison with Literature H-Terminated C(100) and C(111)

Taking the midpoint of BS1 and BS3 as a representative value for H-terminated C(110) gives $\phi_{(110)} \approx 3.59$ eV and $\chi_{(110)} \approx -1.00$ eV. These can be compared with the values reported by Diederich *et al.* for H-terminated C(100)

and C(111), which lie in the range $\phi \approx 3.9 - 4.2\,\text{eV}$ and $\chi \approx -0.9$ to $-1.0\,\text{eV}$ [25]. The C(110) work function is therefore slightly below the literature range, while the NEA is comparable to established values. There is no evidence that H-termination is more effective on C(110) than C(100) and C(111), however it achieved a comparable NEA, work function uniformity, and a significantly lower ϕ. These results demonstrate H-terminated C(110) to be a consistent and competitive platform for producing low-ϕ, NEA diamond surfaces.

4.3 Oxygen Treatment of C(110): Surface Chemistry and the Role of the NEG

Following the analysis of H-termination in Section 4.2, BS1 was subjected to a 900^{o}C UHV anneal alongside the newly installed NEG pump, followed by an initial oxygen treatment (XPS.3 in Figure 15). This section first characterises the surface chemistry produced by oxygen treatment of C(110) in comparison with the H-terminated state. Second, the effective oxygen coverage is assessed against two reference points, including the C(100) results of Zulkharnay *et al.* [13], which test whether oxygen uptake is more favourable on C(110) or C(100), and the previous year's C(110) coverage results from Pritchard-Cairns [53], obtained without a NEG, which test whether the NEG has improved surface preparation on this orientation.

Oxygen coverage was calculated from the fitted XPS peak areas using Equation 7,

$$\text{O\%} = \frac{\dfrac{A_O}{\text{RSF}_O}}{\dfrac{A_C}{\text{RSF}_C} + \dfrac{A_O}{\text{RSF}_O}}. \tag{7}$$

where A_O and A_C are the total integrated areas of the O 1s and C 1s spectra, and $RSF_O = 2.93$ and $RSF_C = 1.00$ are the relative sensitivity factors of O 1s and C 1s [13, 54].

The relevant spectra are the BS1 XPS.3 C 1s and O 1s scans, taken immediately after the first oxygen treatment cycle. They are shown in Figure 22, and the corresponding fitted components, binding energies, peak areas, and relative percentage areas are summarised in Table 5.

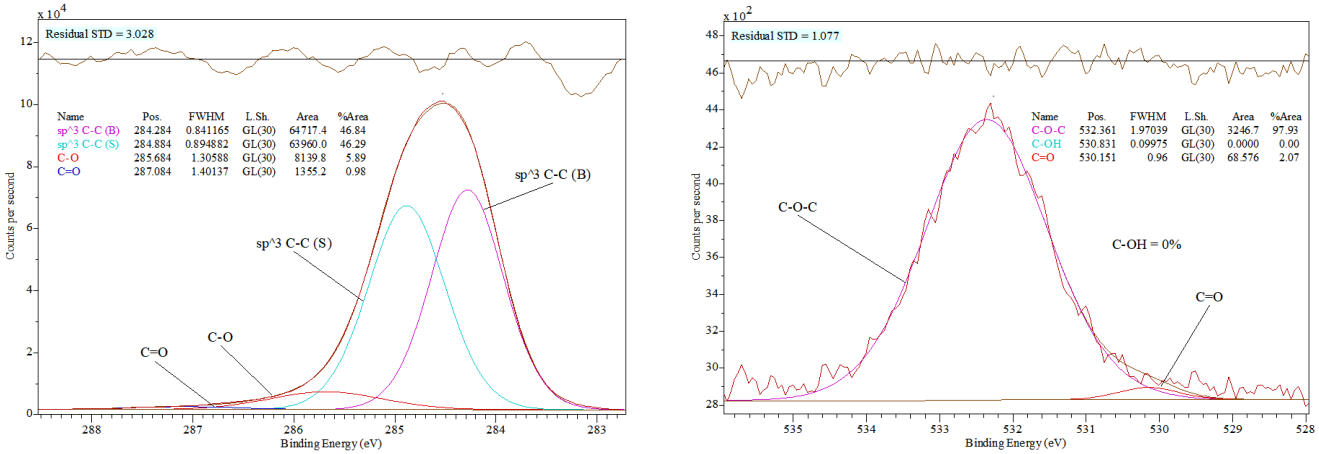

a) BS1 XPS.3 C 1s spectra

b) BS1 XPS.3 O 1s spectra

Figure 22. BS1 O-treated C 1s and O 1s spectra

Element Spectrum	Surface Component	BS1		
		BE (eV)	Area	Rel. (%)
C 1s				
O-treated	sp^3 C–C (B)	284.28	64717.40	46.84
	sp^3 C–C (S)	284.88	63960.00	46.29
	C–O	285.68	8139.80	5.89
	C=O	287.08	1355.20	0.98
O 1s				
O-treated	C–O–C	532.36	3246.70	97.93
	C–OH	530.83	0.00	≈ 0.00
	C=O	530.15	68.58	2.07

Table 5. XPS.3 fitting results for O-treated BDD C(110) surface for BS1, showing the expected surface components, binding energies, peak areas, and relative peak area percentages.

4.3.1 Transition from H-terminated to O-treated C(110)

The noticeable change in the C 1s spectra is the redistribution of the two sp^3 components. In the H-terminated state the bulk sp^3 C-C peak dominated at 86.0% with the surface sp^3 component contributing only 8.3%. After oxygen treatment the two were almost equal in area (46.8% bulk and 46.3% surface), and the overall C 1s core level was visibly broader. As reported by Zulkharnay *et al.* the surface sp^3 fraction reflects the extent of partial oxidation for molecular O_2 treated surfaces, since the pressures used are insufficient to desorb all C-H bonds [13]. The observed high intensity of surface sp^3 may therefore indicate of low oxygen coverage and, more significantly, a failure of the NEG-assisted 900^{o}C anneal to fully contain hydrogen [13]. Alternatively, the apparent increase in surface sp^3 may reflect the removal of non-diamond carbon species, as Osswald *et al.* showed that oxidation preferentially removes sp^2-bonded carbon, including graphitic phases, thereby increasing the relative contribution of sp^3-bonded diamond [55]. The broadening of C 1s core-level likely attributed to surface state formation, band bending and surface roughening associated with oxygen exposure [10]. The C-O contribution rose from 3.7% to 5.9%, confirming increased oxygen incorporation into single-bonded configurations, while the C=O contribution fell from 2.0% to 1.0%.

The O 1s spectra show a rise in the C-O-C component from 94.6% to 97.93% and a drop in C=O from 3.6% to 2.1%, indicating adequate oxygen coverage as supported by DFT calculations [56]. The C-OH contribution fell from 1.83% to effectively zero, an important result demonstrating that the combination of the 900^{o}C anneal and the NEG successfully removed water vapour from the chamber environment, preventing the adsorption of hydroxyl species during the oxygen dose [57]. Without the NEG, residual water vapour would likely re-populate hydroxyl sites, and a C-OH contribution would remain high. The coexistence of C-O-C and C=O is further consistent with the results of Chaudhuri *et al.* [15].

In the O 1s spectra, binding energies shifted downward by $\sim$1 eV after oxygen treatment (e.g. C-O-C from 533.4 eV to 532.4 eV) while the inter-species energy gaps between C-O-C, C-OH, and C=O remained unchanged. This downward shift reflects a change in the electrostatic surface environment rather than a misfit of components. In the H-terminated state, the small amount of oxygen present sat on top of a dipole produced by C-H bonds, which raised the local potential and pushed core levels to higher binding energy. Wan *et al.* showed that after oxygen treatment and removal of H termination, this dipole is replaced by a C-O dipole, with surface oxygen on the negatively charged side and underlying carbon on the positive side, causing the O 1s core levels to shift to lower binding energies while preserving inter-species spacing [10].

4.3.2 Oxygen coverage and the Impact of the NEG

Substituting the fitted areas from Table 5 into Equation 7, with A_O = 3315.28 and A_C= 138172.40, gives an effective oxygen coverage of:

$$O\% \approx 0.81\%.$$

Zulkharnay *et al.* reported 6.47% oxygen coverage on a molecular O_2 treated C(100) surface prepared under comparable conditions, corresponding to 90% of the UV-ozone coverage, assumed to represent full coverage [13]. The C(110) coverage measured here is 13.5% of this value, showing that oxygen uptake is more effective on C(100). The C(110) surface presents a different atomic geometry, with zigzag rows of carbon atoms of lower dangling bond density and angle than C(100), which may account for the limited coverage [2, 15, 16, 22]. This is consistent with the geometric constraint identified by Chaudhuri *et al.*, whose DFT work indicated that C(110) energetically favours a p(2×2) keto-ether reconstruction with a theoretical maximum oxygen coverage of roughly 5.5 atoms/nm^2, translating to 1/4 monolayer coverage (given a carbon dangling bond density of 22.2 atoms/nm^2), substantially below the 90% equivalent achieved by Zulkharnay *et al.* on C(100) [15, 58]. The dominance of stable C-O-C bonding is further beneficial, as it is reported to increase oxygen content more effectively than C=O groups [59].

Pritchard-Cairns reported 2.0% oxygen coverage on a C(110) surface after multiple treatment cycles, without a NEG installed [53]. The present value of 0.81% is lower by 1.2 percentage points. However, the present work applied only a single oxygen treatment cycle, and with the NEG in place coverage would be expected to increase over multiple cycles. However, the low coverage combined with the increased surface sp^3 C-C area in the C 1s spectra may further support the possibility that the NEG failed to fully remove residual hydrogen.

These comparisons show that the O-treatment of C(110) reported here produced a surface with considerably less oxygen coverage than C(100). Zulkharnay *et al.* observed their 90% coverage C(100) surface to lose sufficient NEA after 64 h of air exposure, so the present C(110) surface is likely to meet the same fate, possibly in a shorter duration [13]. However, it may prove chemically better prepared for the subsequent oxygen-lithium termination sequence than any prior C(110) result obtained without a NEG.

4.4 SPA-LEED: Surface Order Before and After Annealing

SPA-LEED was used to assess the long-range crystalline order of C(110) and to test whether the 900^{o}C anneal improved surface order or revealed any evidence of the relaxed (1×1) zigzag row geometry expected for a clean, dehydrogenated C(110) surface [16]. Each measurement was taken at two incident energies, including 96 and 144 eV before annealing, and 92 and 148 eV after. The lower energy in each pair maximised surface sensitivity, while the higher provided sharper, deeper-probed spots [46, 14]. A well-ordered, smooth C(110) surface would be expected to produce a rectangular pattern of sharp, high intensity spots on a low diffuse background [10, 45, 46].

The pre-anneal images at 96 and 144 eV are shown in Figure 23, and the post-anneal images at 92 and −1.07 eV in Figure 24.

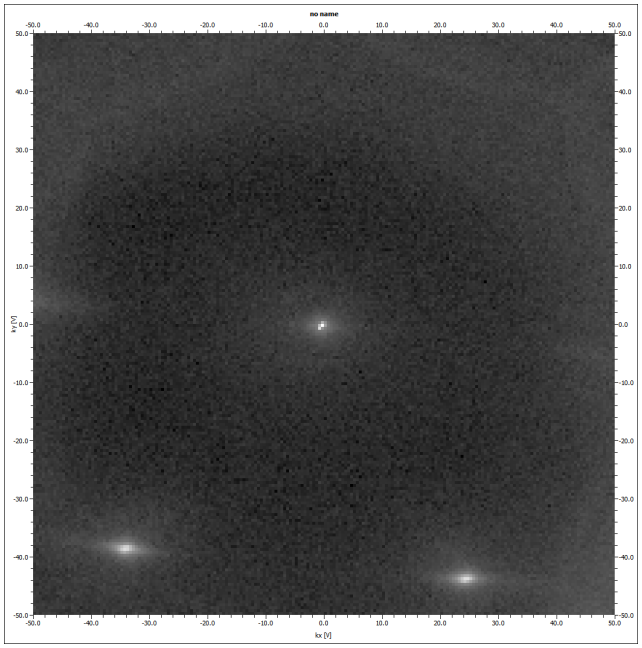

a) BS1 LEED.1 96 eV LEED spot image

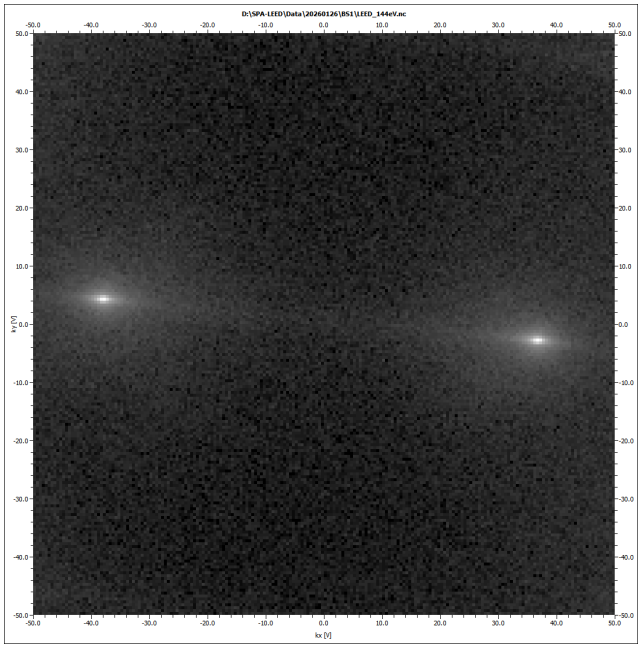

b) BS1 LEED.1 144 eV LEED spot image

Figure 23. BS1 SPA-LEED images at two distinct electron energies (before 900^{o}C anneal).

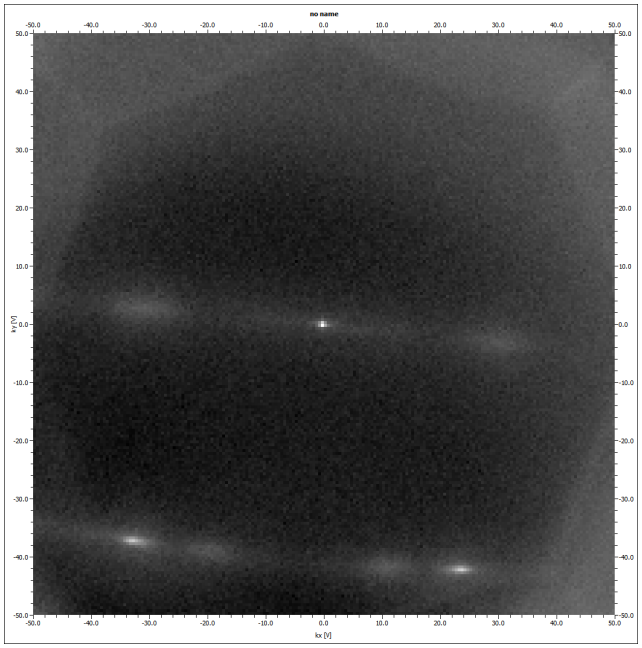

a) BS1 LEED.1 92 eV LEED spot image

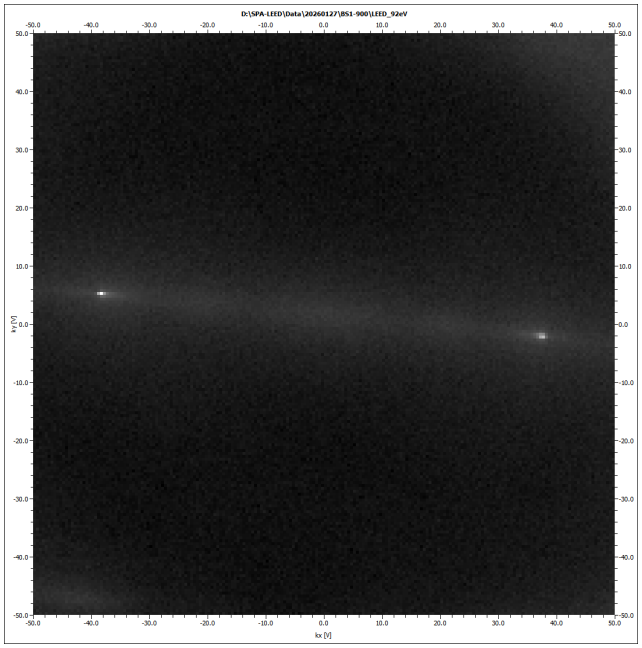

b) BS1 LEED.1 144 eV LEED spot image

Figure 24. BS1 SPA-LEED images at two distinct electron energies (after 900^{o}C anneal).

Before annealing, the 96 eV image showed broad, low intensity spots on a diffuse background, consistent with a rough, disordered surface. After the 900^{o}C anneal, the 92 eV image showed narrower, more intense spots with reduced background, indicating a well-ordered, smoother surface, potentially due to hydrogen desorption [10, 45, 46, 47]. The higher-energy images (144 and 148eV) follow exactly the same trend, and because they probe deeper into the near-surface region, this reflects an improvement of crystalline order throughout the material layers.

The post-anneal pattern was not of sufficient quality to support spot profile analysis or to identify a relaxed C(110)-(1×1) reconstruction. This is in line with literature, which states that LEED on C(110) is more difficult to achieve than on other orientations [14]. The main result is therefore that the observation of a resolvable diffraction pattern at multiple energies is sufficient to confirm a long-range crystalline order. Hydrogen exposure of C(110) has been reported to produce surface defects that contribute to a more diffuse LEED background, so the reduced

background observed here implies that the 900^{o}C anneal effectively removed hydrogen [47].

4.5 Oxygen-Lithium Functionalisation: Chemical and Electronic Evolution

This section observes the evolution of the surface chemistry (via XPS) and electronic properties (via EF-PEEM and UPS) of BS1 across three oxygen-lithium termination cycles, labelled XPS.4, XPS.5, and XPS.6 in Figure 15. The O-treated XPS.3 surface characterised in Section 4.3 serves as the zero-lithium reference. The two objectives are to establish how the O-Li surface dipole develops with repeated cycles and whether saturation occurs, and to compare the final lithiated C(110) surface against the lithiated C(100) results of Zulkharnay *et al.* to determine whether C(110) is a competitive orientation for strong O-Li dipole formation [13].

4.5.1 Evolution of O 1s and Li 1s Spectra Across Three Cycles

Figures 25, 26 and 27 show the fitted O 1s and Li 1s spectra after cycles 1, 2, and 3 respectively. All fitted components, binding energies, absolute areas, and relative areas are displayed in Table 6. Peak assignments follow the same scheme used in Sections 4.2 and 4.3, with the addition of two new lithium components, including C-O-Li and li_2O.

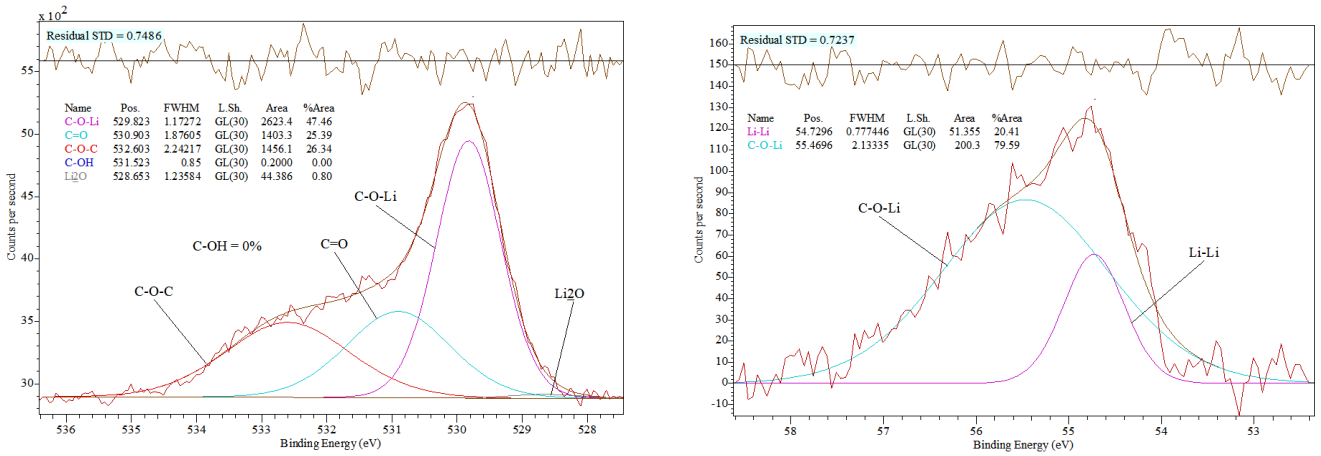

a) BS1 XPS.4 O 1s spectra

b) BS1 XPS.4 Li 1s spectra

Figure 25. BS1 XPS.4 O 1s and Li 1s after the 1st complete cycle of O-Li termination.

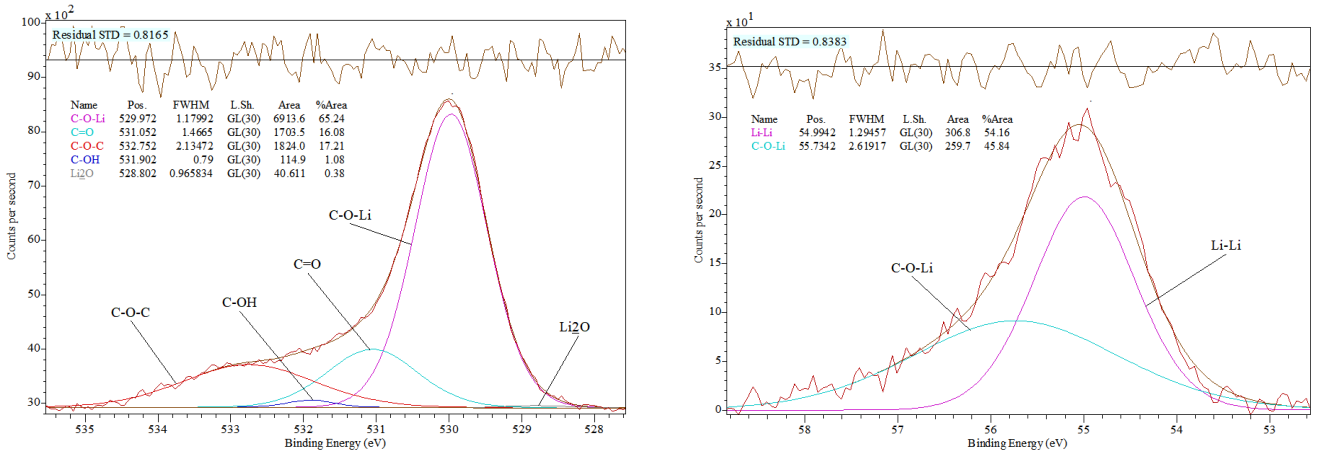

a) BS1 XPS.5 O 1s spectra

b) BS1 XPS.5 Li 1s spectra

Figure 26. BS1 XPS.5 O 1s and Li 1s after the 2nd complete cycle of O-Li termination.

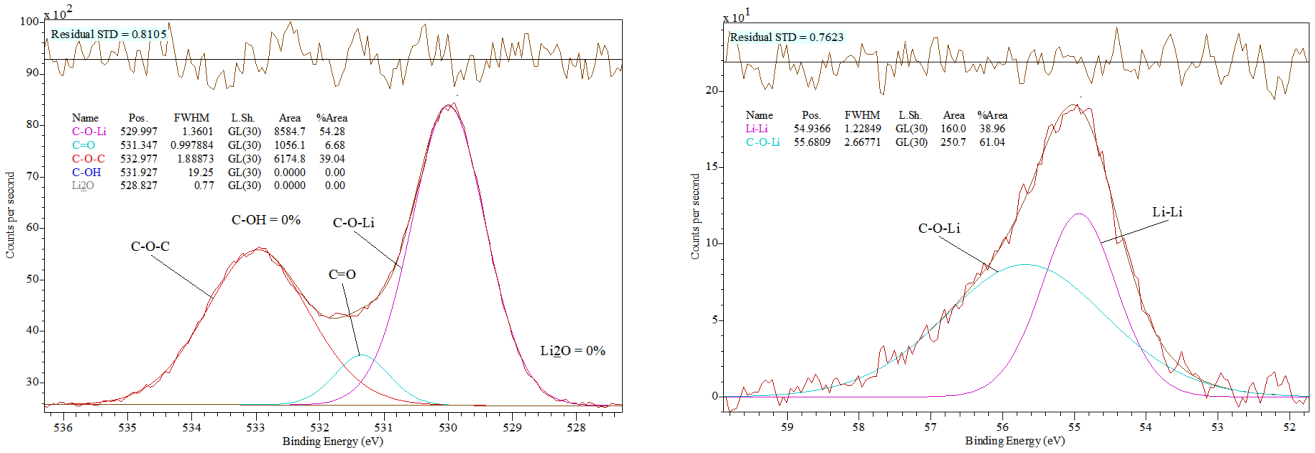

a) BS1 XPS.6 O 1s spectra

b) BS1 XPS.6 Li 1s spectra

Figure 27. BS1 XPS.6 O 1s and Li 1s after the 3rd complete cycle of O-Li termination.

Element Spectrum	Surface Component	XPS.4 (1st cycle)			XPS.5 (2nd cycle)			XPS.6 (3rd cycle)		
		BE (eV)	Area	Rel. (%)	BE (eV)	Area	Rel. (%)	BE (eV)	Area	Rel. (%)
O 1s										
Lithiated	C–O–Li	529.82	2623.40	47.46	529.97	6913.60	65.24	530.00	8584.70	54.28
	C=O	530.90	1403.30	25.39	531.05	1703.50	16.08	531.35	1056.10	6.68
	C–O–C	532.60	1456.10	26.34	532.75	1824.00	17.21	532.98	6174.80	39.04
	C–OH	531.52	0.20	≈ 0	531.90	114.90	1.08	531.93	≈ 0	≈ 0
	Li_2O	528.65	44.39	0.80	528.80	40.61	0.38	528.83	≈ 0	≈ 0
Li 1s	Li–Li	54.73	51.36	20.41	54.99	306.80	54.16	54.94	160.00	38.96
	C–O–Li	55.47	200.30	79.59	55.73	259.70	45.84	55.68	250.70	61.04

Table 6. XPS fitting results for O 1s and Li 1s spectra across successive oxygen–lithium termination cycles (XPS.4–XPS.6), showing binding energies, peak areas, and relative peak area percentages.

XPS.3 → XPS.4: Appearance of O-Li Bonding and Dipole Reversal

The O-treated XPS.3 surface showed an O 1s spectrum dominated by C-O-C at 532.36 eV (97.93%), with a small C=O contribution (2.1%) and essentially no C-OH or Li-related components. After the first lithium deposition cycle (XPS.4), two new components appear, including C-O-Li at 529.82 eV (47.5%) and a small Li_2O feature at 528.65 eV (0.8%). Oxygen groups were also redistributed, with C-O-C falling from 97.9% to 26.3% and C=O rising from 2.1% to 25.4%. Lithium reacted with C-O-C to form the C-O-Li bond, while the growth of C=O reflects increased molecular O_2 exposure.

The Li 1s spectrum at this stage was dominated by C-O-Li (79.6%, area 200.3) with only a small metallic Li-Li component (20.41%, area 51.4), confirming that the first cycle deposited lithium predominantly in bonded rather than metallic cluster form [13].

XPS.4 → XPS.5: Dipole Strengthening and Start of Metallic Clustering.

After the second cycle, the O 1s C-O-Li component grew from 47.5% to 65.2% and its area increased from 2623 to 6914, a factor of 2.6, confirming continued Li incorporation into oxygen bonding sites. Both C=O (25.4% → 16.1%) and C-O-C (26.3% → 17.2%) fell as the C-O-Li bonds dominated. A small C-OH component (1.1%) reappeared, most likely from a misfit or minor water vapour exposure during the dosing in the FEL chamber.

The Li 1s spectrum underwent a more significant change. The Li-Li area grew from 51.4 to 306.8 (a factor of ∼6), while the C-O-Li area grew from 200.3 to 259.7 (a factor of 1.3). Li-Li then dominated the Li 1s spectra at 54.2% against 45.8%. This most likely reflects the process of metallic lithium clustering as the first cycle saturated nearly all present oxygen sites, so additional Li deposited in the second cycle had no remaining chemical sites and settled as metallic clusters on top of the bonded layer [13]. The C-O-Li channel was still growing in absolute terms, so

the dipole continued to strengthen, but the efficiency of lithium deposition had decreased.

XPS.5 → XPS.6: Saturation of C-O-Li and Recovery from Clustering.

After the third cycle, the O 1s C-O-Li area grew only from 6914 to 8585, a factor of 1.2, while C-O-C reappeared strongly (17.2% → 39.0%). This indicates C-O-Li saturation after the second cycle, with lithium limited by the available bonding sites, and additional oxygen incorporated as C-O-C instead. The slower growth of C-O-Li despite a third full Li dose also supports this idea. C=O fell further to 6.7%, while C-OH and Li_2O were both effectively removed: C-OH by successive 500^{o}C activation anneals, consistent with the lower adsorption energy of hydroxyl groups relative to ether and ketone groups, calculated by Petrini and Larsson, and Li_2O likely converted into C-O-Li [60].

The Li 1s spectrum also stabilised. The Li-Li area decreased from 306.8 to 160.0 (a factor of 1.9), suggesting reformation of metallic clusters into O-Li bonds, while the C-O-Li area was essentially unchanged (259.7 → 250.7) but re-dominated at 61.04% area percentage. The third cycle therefore produced a cleaner, more ordered Li-bonded surface with reduced metallic cluster content, even though the total C-O-Li coverage had plateaued.

Spectral Shifts

Ullah *et al.* reported that O 1s core-level peaks shift to higher binding energies at temperatures above ∼ 850^{o}C, corresponding to lithium desorption and loss of the O-Li dipole. Increased lithium should therefore shift peaks to lower binding energies, as charge transfer from Li to O produces a more negative potential on O atoms [61]. A similar effect applies to C 1s [61].

Figure 28 shows the core-level binding energy shifts for C 1s and O 1s spectra across three cycles.

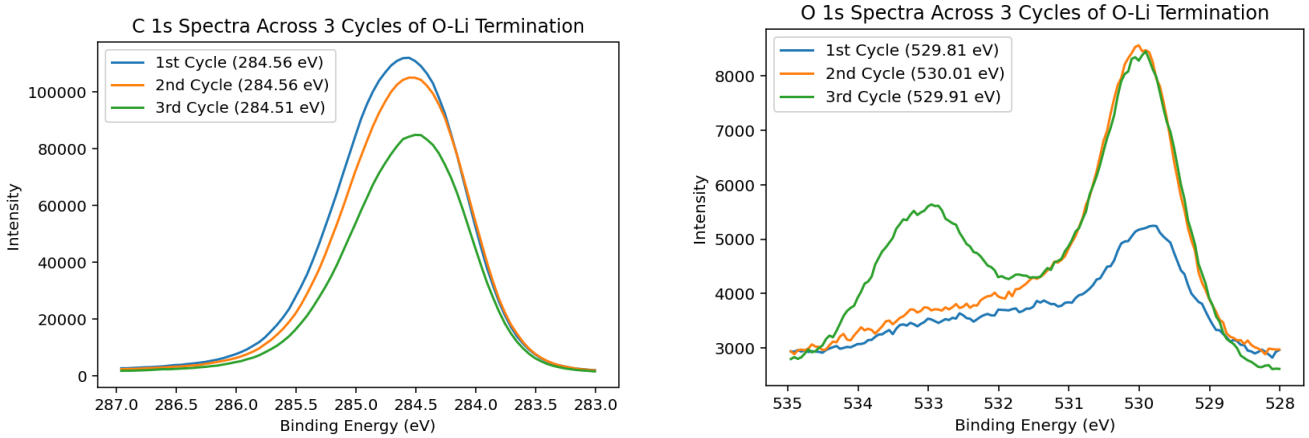

a) C 1s core-level spectral shift

b) O 1s core-level spectral shift

Figure 28. Core-level peaks for C 1s and O 1s across three oxygen-lithium termination cycles

The expected reduction in C 1s peak area across cycles was observed. For the dominant O 1s peak (C-O-Li), intensity increased significantly after the first cycle and was then almost identical between second and third cycles. This further supports C-O-Li saturation after the second cycle, consistent with the minor difference in Li 1s C-O-Li areas between cycle 2 and 3.

No lowering of binding energies was observed from the first to the final cycle for either C 1s or O 1s. The C 1s, values fell between 284.51 eV and 284.56 eV, a negligible difference, and the O 1s increased from 529.81 eV to 530.01 eV between cycles 1 and 2 before falling back to 529.91 eV at cycle 3. This lack of correlation may reflect inaccuracies in peak-component assignment or, more likely, the method of lithium control as Ullah *et al.* used thermally controlled lithium desorption, whereas the present method added lithium by deposition followed by 500^{o}C activation annealing.

Comparison with Lithiated C(100)

The cycle-3 C(110) surface can now be compared against the lithiated molecular O_2 treated C(100) results in Table 2. The most obvious difference is in the C-O-Li contribution to the O 1s spectrum, 54.28% on C(110) against 13.6% on C(100). The C(110) surface also showed more C-O-C (39.0% vs 11.0%) and, critically, near-zero C-OH against the 28.6% hydroxyl contribution reported on C(100). The large C(100) C-OH fraction is a sign of water vapour presence during or after dosing, which the present work avoided, most likely as a result of the NEG installation prior to the 900^{o}C anneal. The C(110) surface was therefore contained a stronger amount of C-O-Li. The Li 1s spectra were comparable as Zulkharnay *et al.* reported 32.1% Li-Li and 67.9% C-O-Li, against 39.0% and 61.0% here. The variation of lithium between metallic and bonded channels was therefore roughly equivalent on the two orientations, but the O 1s evidence strongly favours C(110) for C-O-Li formation, most likely because of the different atomic geometry and bonding site density of the C(110) plane combined with the NEG-assisted UHV environment [22].

4.5.2 Work Function and NEA Across Cycles

EF-PEEM and UPS were recorded after cycle 1 (corresponding to XPS.4) and after cycle 3 (corresponding to XPS.6). No photoemission data were recorded after cycle 2, so the XPS.5 discussion above remains unverified. The work function maps and histograms are shown in Figures 29 and 30, the corresponding UPS spectra in Figures 31 and 32, and the extracted parameters in Table 7.

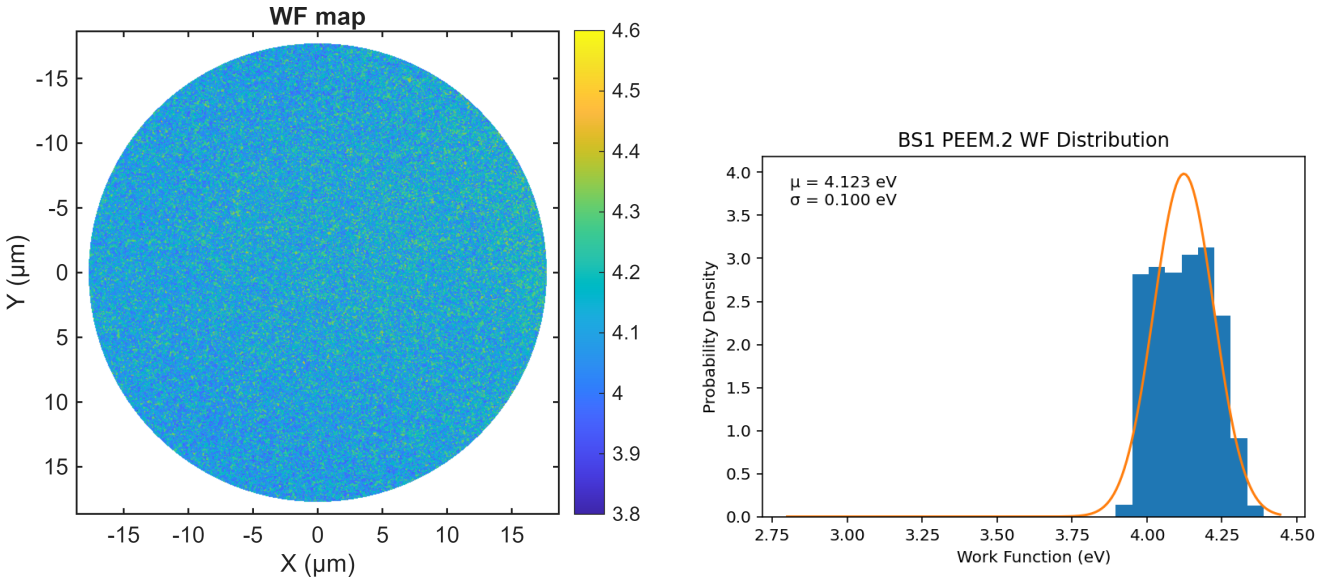

a) BS1 EF-PEEM.2 work function variation map

b) BS1 EF-PEEM.2 work function distribution histogram

Figure 29. BS1 oxygen-lithium terminated work function variation map and distribution histogram after the 1st cycle.

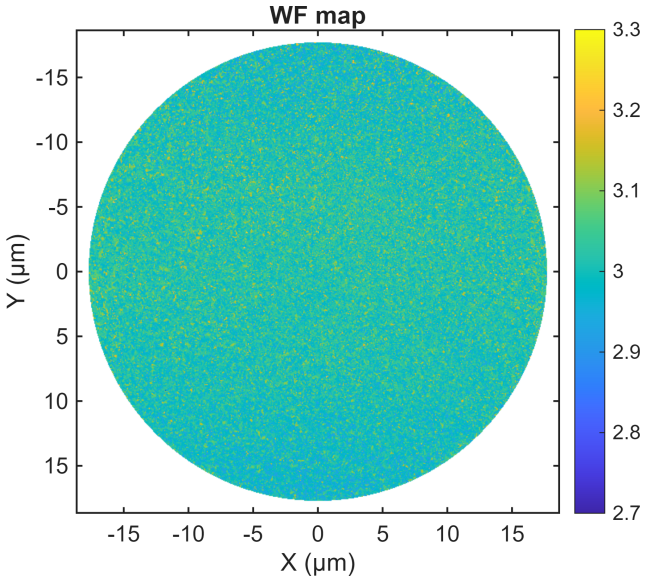

a) BS1 EF-PEEM.3 work function variation map

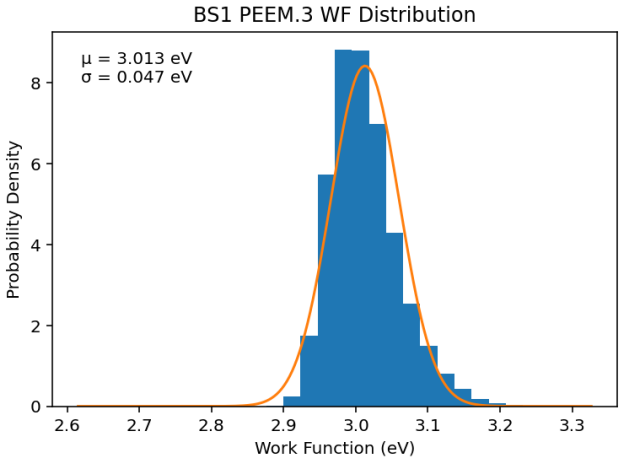

b) BS1 EF-PEEM.3 work function distribution histogram

Figure 30. BS1 oxygen-lithium terminated work function variation map and distribution histogram after 3rd and final cycle.

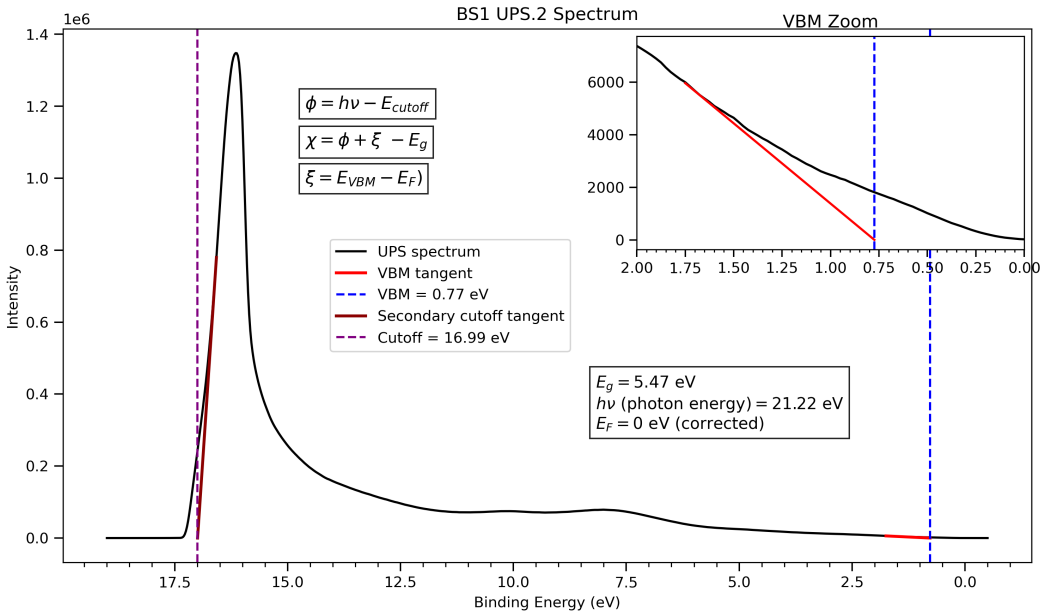

Figure 31. Corresponding UPS.2 spectra to Figure 28 EF-PEEM.2 results.

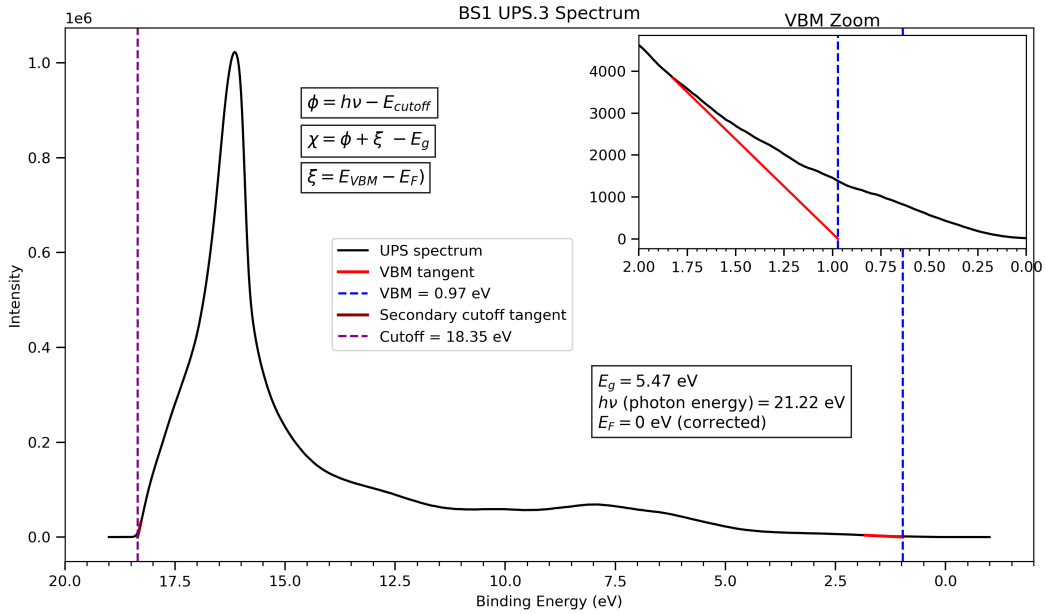

Figure 32. Corresponding UPS.3 spectra to Figure 29 EF-PEEM.3 results.

Technique	Parameter (eV)	Sample (BS1)	
		1st cycle	3rd cycle
EF-PEEM	Mean ϕ	4.12	3.01
	Standard Deviation, σ	0.10	0.05
UPS	E_{SECO}	16.99	18.35
	E_{VBM}	0.77	0.97
	ϕ	4.23	2.87
	χ	-0.58	-1.49

Table 7. Summary of EF-PEEM and UPS results for oxygen-lithium terminated BS1 samples after the 1st cycle and after the final 3rd cycle, showing work function statistics and electronic structure parameters.

Cycle 1: Oxygen-Dominated, Weakly NEA.

After cycle 1, $\phi = 4.12\,\mathrm{eV}$ and $\chi = -0.58\,\mathrm{eV}$, a substantial increase in ϕ relative to the H-terminated baseline (3.64eV) and a much weaker NEA than the H-terminated result (-1.07eV). This is consistent with the XPS.4 chemistry as although C-O-Li was present at 47.46%, C=O and C-O-C together still contributed over 50%, and the more electronegative oxygen in these bonds raised the local vacuum level. The surface at this stage was chemically a hybrid, neither fully oxygen-terminated (PEA-like) nor fully Li-dominated, and its electronic behaviour sat between the two. The work function standard deviation was $\sigma = 0.10\,\mathrm{eV}$, five times larger than the H-terminated value of $0.02\,\mathrm{eV}$, confirming that the O-Li dipole is not yet spatially uniform. This non-uniformity in the work function maps is a result of partial O-Li coverage and the formation of metallic Li-Li clusters [13]. In regions of higher Li coverage the dipole was established and ϕ locally lower, while in regions still dominated by residual C=O and C-O-C the vacuum level remained above the CBM, giving a higher local ϕ.

Expected Behaviour at Cycle 2

Although no PEEM or UPS data were recorded after cycle 2, the XPS.5 chemistry suggests an intermediate ϕ and NEA. Two competing effects would be in play as the Li 1s C-O-Li absolute area was highest at cycle 2 (259.7, vs 79.6 at cycle 1 and 250.7 at cycle 3), which should produce a strong dipole similar to the final cycle, however, Li-Li metallic clustering was also at its peak (54.2%), and reduction of the C-O-Li component by clustered Li could

have reduced the overall dipole strength. The likely outcome is a surface with a strong but spatially inconsistent ϕ, with the largest σ of the three cycles [13].

Cycle 3: Li-dominated, Strong NEA

After the third cycle, ϕ fell to 3.01 eV and χ increased in magnitude to -1.49 eV, a 1.11 eV reduction in ϕ and near-tripling of NEA relative to cycle 1. This aligns with the XPS.6 results as C-O-Li dominated the O 1s spectrum at 54.28%, metallic Li-Li had reduced from 54.2% to 39.0% of the Li 1s signal, and the dipole layer was uniform enough to halve σ to 0.05 eV.

An alternative interpretation, following O'Donnell *et al.*, is that the progressive NEA improvement across cycles reflects a thermally activated reorganisation of the O–Li layer rather than an increase in C–O–Li density [31]. Annealing of lithiated C(100) up to 800^{o}C was shown to improve NEA, suggesting that dipole formation is an energy-activated process [31]. The repeated exposure of BS1 to 500^{o}C anneals between cycles may therefore have guided structural reorganisation of the O–Li layer into a more favourable configuration, consistent with the reduction in metallic Li–Li clustering observed after cycle 3 [31]. The transition from cycle 1 to cycle 3 therefore represents an improvement from a hybrid surface with insufficient dipole and weak NEA (tending toward PEA) to a Li-dominated surface with strong NEA, lead by the growth and stabilisation of C-O-Li bonding, combined with thermally-activated reorganisation.

Comparison with H-terminated C(110) and Lithiated C(100)

Compared to the H-terminated C(110) results of Section 4.2.2 ($\phi = 3.64$ eV, $\chi = -1.07$ eV), the cycle 3 O-Li surface showed both a lower ϕ (3.01 vs 3.64 eV) and a stronger NEA (-1.49 vs -1.07 eV). This shows that engineered O-Li functionalisation on C(110) is not only an alternative to H-termination but outperforms it in both key areas. The C-O-Li dipole is stronger than the C-H dipole and produces a more efficient emission surface, whilst also proven to remain stable up to 850^{o}C [61].

Comparison with the lithiated C(100) value of $\chi = -1.68$ eV reported by Zulkharnay *et al.* positions the cycle 3 C(110) surface 0.19 eV behind the C(100) reference [13]. This could reflect a limitation of the C(110) orientation, but XPS evidence shows that the C(110) surface achieved a much higher C-O-Li fraction (54.3% vs 13.6%) and was free of hydroxyl formation, while the C(100) produced a greater C-OH component. The C-O-Li area on C(110) appears to have saturated by cycle 2, suggesting the dipole layer was limited not by a shortage of Li but by a shortage of bonding sites, which could be increased by repeating the oxygen treatment steps prior to lithium deposition. The $\sigma = 0.05$ eV uniformity achieved at cycle 3 suggests there is little room for improved dipole uniformity, so the 0.19 eV gap to C(100) is likely dominated by dipole strength rather than uniformity. Optimising the oxygen pre-treatment to maximise the density of ether bridges available for Li bonding is therefore the most likely route to closing this gap.

5. Conclusion

This project aimed to observe the relationship between surface chemistry and electronic properties of boron-doped C(110) diamond, while producing low work function NEA surfaces suitable for next-generation electron emission devices. Two MPCVD-grown samples were analysed by XPS, EF-PEEM, UPS, and SPA-LEED across H-terminated, O-treated, and oxygen–lithium terminated configurations, with a NEG pump installed to improve UHV quality during functionalisation steps.

H-terminated C(110) was consistent between BS1 and BS3, with sp^3 fractions aligning within 2 percentage points and binding energies agreeing within 0.1 eV. The average values of $\phi \approx 3.59$ eV and $\chi \approx -1.00$ eV place C(110) as comparable with the literature range for H-terminated C(100) and C(111), with a comparable NEA and high degree of spatial uniformity ($\sigma = 0.02$ eV). Future work should look to extend this comparison to a larger sample set to establish statistical reproducibility rather than consistency between two measurements.

Oxygen treatment produced a surface dominated by C–O–C bonding (97.9%) with very little C–OH, showing that

the NEG removed water vapour. However, the effective oxygen coverage of 0.81% was much lower than the 6.47% achieved by Zulkharnay *et al.* on C(100) and the 2.0% reported by Pritchard-Cairns on C(110) without a NEG, suggesting the 900^{o}C anneal may not have removed hydrogen completely. Future work should look to optimise the oxygen dosing parameters, while applying multiple treatment cycles to improve the density of C-O-C available for lithium bonding into C-O-Li.

SPA-LEED confirmed that the 900^{o}C anneal improved long-range crystalline order, with sharper spots and reduced background at both energies. The post-anneal pattern was insufficient to support full spot-profile analysis or identify a relaxed (1×1) reconstruction, consistent with the reported literature on C(110). Future work should focus on improving surface quality during the growth stage, allowing more effective SPA-LEED analysis.

Three oxygen–lithium cycles produced a Li-dominated surface with $\chi = -1.49\,\mathrm{eV}$ and $\phi = 3.01\,\mathrm{eV}$, surpassing the H-terminated C(110) results in both areas and producing a higher C–O–Li fraction (54.3%) than the lithiated C(100) of Zulkharnay *et al.* (13.6%). C–O–Li bonding appeared to saturate after the second cycle, leaving a $0.19\,\mathrm{eV}$ gap to the C(100) reference of $-1.68\,\mathrm{eV}$ that is most likely limited by available bonding sites rather than dipole uniformity. Future work should improve the oxygen pre-treatment to increase C-O-C density and test the thermal and atmospheric stability of the surface against the 64 h air exposure to provide further comparisons against Zulkharnay *et al.* C(100) results.

This work shows that O–Li functionalisation on C(110), accompanied by NEG-supported UHV conditions, produces a thermally stable, low work function NEA surface that competes with the established C(100) results. C(110) therefore represents a promising surface for application in reproducible vacuum electronic devices.

References

[1] D. M. Trucchi and N. A. Melosh, "Electron-emission materials: Advances, applications, and models," *MRS Bull.*, vol. 42, no. 7, pp. 488–492, 2017. [Accessed: 18-Mar-2026].

[2] M. C. James, F. Fogarty, R. Zulkharnay, N. A. Fox, and P. W. May, "A review of surface functionalisation of diamond for thermionic emission applications," *Carbon*, vol. 171, pp. 532–550, 2021. [Accessed: 25-Mar-2026].

[3] A. Kahn, "Fermi level, work function and vacuum level," *Mater. Horiz.*, vol. 3, pp. 7–10, 2016. [Accessed: 14-Mar-2026].

[4] D. B. Go *et al.*, "Thermionic energy conversion in the twenty-first century," *Front. Mech. Eng.*, vol. 3, p. 13, 2017. [Accessed: 02-Apr-2026].

[5] A. Croot, G. Wan, A. Rowan, H. D. Andrade, J. A. Smith, and N. A. Fox, "Beta radiation enhanced thermionic emission from diamond thin films," *Front. Mech. Eng.*, vol. 3, p. 17, 2017. [Accessed: 21-Mar-2026].

[6] H. Kagan, "Diamond radiation detectors may be forever!," Dept. of Physics, Ohio State Univ., Columbus, OH, USA, 2005. [Accessed: 16-Mar-2026].

[7] R. Zulkharnay and P. W. May, "Experimental evidence for large negative electron affinity from scandium-terminated diamond," *J. Mater. Chem. A*, vol. 11, pp. 13432–13445, 2023. [Accessed: 28-Mar-2026].

[8] K. M. O'Donnell, T. L. Martin, N. A. Fox, and D. Cherns, "Ab initio investigation of lithium on the diamond C(100) surface," *Phys. Rev. B*, vol. 82, p. 115303, 2010. [Accessed: 15-Mar-2026].

[9] M. C. James, P. W. May, A. Croot, and N. L. Allan, "A theoretical study of negative electron affinity from aluminium on the diamond (100) surface," *J. Phys.: Condens. Matter*, vol. 30, p. 235002, 2018. [Accessed: 30-Mar-2026].

[10] G. Wan, M. Cattelan, and N. A. Fox, "Electronic structure tunability of diamonds by surface functionalization," *J. Phys. Chem. C*, vol. 123, pp. 4168–4177, 2019. [Accessed: 19-Mar-2026].

[11] F. Maier, J. Ristein, and L. Ley, "Electron affinity of plasma-hydrogenated and chemically oxidized diamond (100) surfaces," *Phys. Rev. B*, vol. 64, p. 165411, 2001. [Accessed: 04-Apr-2026].

[12] R. Zulkharnay, N. A. Fox, and P. W. May, "Enhanced electron emission performance and air-surface stability in ScO-terminated diamond for thermionic energy converters," *Small*, vol. 20, p. 2405408, 2024. [Accessed: 22-Mar-2026].

[13] R. Zulkharnay, W. Greenwood, A. Wood, J. Laverock, and N. A. Fox, "Achieving a large net 'negative electron affinity' on diamond (100) via molecular oxygen and lithium functionalization," *ACS Appl. Mater. Interfaces*, vol. 18, pp. 9032–9042, 2026. [Accessed: 05-Apr-2026].

[14] P. K. Baumann and R. J. Nemanich, "Surface cleaning, electronic states and electron affinity of diamond (100), (111) and (110) surfaces," *Surf. Sci.*, vol. 409, pp. 320–335, 1998. [Accessed: 17-Mar-2026].

[15] S. Chaudhuri, S. J. Hall, B. P. Klein, M. Walker, A. J. Logsdail, J. V. Macpherson, and R. J. Maurer, "Coexistence of carbonyl and ether groups on oxygen-terminated (110)-oriented diamond surfaces," *Commun. Mater.*, vol. 3, p. 6, 2022. [Accessed: 31-Mar-2026].

[16] M. De La Pierre, M. Bruno, C. Manfredotti, F. Nestola, M. Prencipe, and C. Manfredotti, "The (100), (111) and (110) surfaces of diamond: An ab initio B3LYP study," *Mol. Phys.*, vol. 112, no. 7, pp. 1030–1039, 2014. [Accessed: 23-Mar-2026].

[17] E. B. Agyekum, "Beta-voltaic nuclear batteries – review of recent developments, challenges and future research directions," *J. Energy Storage*, vol. 122, p. 116701, 2025. [Accessed: 27-Mar-2026].

[18] G. R. Mackenzie *et al.*, "A diamond gammavoltaic cell utilizing surface conductivity and its response to different photon interaction mechanisms," *Mater. Today Energy*, vol. 21, p. 100688, 2021. [Accessed: 20-Mar-2026].

[19] G. Wan, M. Cattelan, A. Croot, H. Dominguez-Andrade, S. S. Nicley, K. Haenen, and N. A. Fox, "Spectroscopic insight of low energy electron emission from diamond surfaces," *Carbon*, vol. 185, pp. 376–383, 2021. [Accessed: 01-Apr-2026].

[20] N. L. Allan and P. W. May, "A hybrid density functional theory investigation of silicon and germanium at the (100) diamond surface: Routes to stable negative electron affinity for electron-emission applications," *Appl. Surf. Sci.*, vol. 717, p. 164732, 2026. [Accessed: 14-Mar-2026].

[21] J. Ristein, "Surface science of diamond: Familiar and amazing," *Surf. Sci.*, vol. 600, pp. 3677–3689, 2006. [Accessed: 29-Mar-2026].

[22] T. L. Martin, "Lithium oxygen termination as a negative electron affinity surface on diamond: A computational and photoemission study," Ph.D. dissertation, School of Physics, Univ. of Bristol, Bristol, U.K., 2011. [Accessed: 24-Mar-2026].

[23] F. J. Himpsel, J. A. Knapp, J. A. Van Vechten, and D. E. Eastman, "Quantum photoyield of diamond (111) – A stable negative-affinity emitter," *Phys. Rev. B*, vol. 20, p. 624, 1979. [Accessed: 26-Mar-2026].

[24] J. van der Weide, Z. Zhang, P. K. Baumann, M. G. Wensell, J. Bernholc, and R. J. Nemanich, "Negative-electron-affinity effects on the diamond (100) surface," *Phys. Rev. B*, vol. 50, no. 8, pp. 5803–5806, 1994. [Accessed: 03-Apr-2026].

[25] L. Diederich, O. M. Küttel, P. Aebi, and L. Schlapbach, "Electron affinity and work function of differently oriented and doped diamond surfaces determined by photoelectron spectroscopy," *Surf. Sci.*, vol. 418, no. 1, pp. 219–239, 1998. [Accessed: 18-Mar-2026].

[26] F. Zhao *et al.*, "A review of diamond materials and applications in power semiconductor devices," *Materials*, vol. 17, p. 3437, 2024. [Accessed: 21-Mar-2026].

[27] P. W. May, W. J. Ludlow, M. Hannaway, P. J. Heard, J. A. Smith, and K. N. Rosser, "Raman and conductivity studies of boron doped microcrystalline diamond, facetted nanocrystalline diamond and cauliflower diamond films," *Diamond Relat. Mater.*, vol. 17, pp. 105–117, 2008. [Accessed: 30-Mar-2026].

[28] M. Sobaszek, Ł. Skowroński, R. Bogdanowicz, K. Siuzdak, A. Cirocka, P. Zieba, M. Gnyba, M. Naparty, Ł. Gołuński, and P. Płotka, "Optical and electrical properties of ultrathin transparent nanocrystalline boron-doped diamond electrodes," *Opt. Mater.*, vol. 42, pp. 24–34, 2015. [Accessed: 16-Mar-2026].

[29] Y. Gong, Y. Wang, Z. Liu, X. Zhang, J. Zhao, and Y. Tang, "Effect of boron doping levels on the microstructure and characteristics of high-quality boron-doped diamond electrodes prepared by MPCVD," *Diamond Relat. Mater.*, vol. 139, p. 110377, 2023. [Accessed: 02-Apr-2026].

[30] F. Fogarty, N. A. Fox, and P. W. May, "Experimental studies of electron affinity and work function from titanium on oxidised diamond (100) surfaces," *Funct. Diamond*, vol. 2, pp. 103–111, 2022. [Accessed: 25-Mar-2026].

[31] K. M. O'Donnell, T. L. Martin, M. T. Edmonds, A. Tadich, L. Thomsen, J. Ristein, C. I. Pakes, N. A. Fox, and L. Ley, "Photoelectron emission from lithiated diamond," *Phys. Status Solidi A*, vol. 211, pp. 2209–2222, 2014. [Accessed: 28-Mar-2026].

[32] R. Zulkharnay, G. Zulpukarova, and P. W. May, "Oxygen-terminated diamond: Insights into the correlation between surface oxygen configurations and work function values," *Appl. Surf. Sci.*, vol. 658, p. 159776, 2024. [Accessed: 15-Mar-2026].

[33] K. M. O'Donnell, T. L. Martin, and N. L. Allan, "Light metals on oxygen-terminated diamond (100): Structure and electronic properties," *Chem. Mater.*, vol. 27, pp. 1306–1315, 2015. [Accessed: 04-Apr-2026].

[34] R. J. Nemanich, J. A. Carlisle, A. Hirata, and K. Haenen, "CVD diamond – Research, applications, and challenges," *MRS Bull.*, vol. 39, pp. 490–494, 2014. [Accessed: 19-Mar-2026].

[35] J. Wang, G. Zhang, N. Chen, M. Zhou, and Y. Chen, "A review of tool wear mechanism and suppression method in diamond turning of ferrous materials," *Int. J. Adv. Manuf. Technol.*, vol. 113, pp. 1–23, 2021. [Accessed: 22-Mar-2026].

[36] G. Alba, M. P. Villar, R. Alcántara, J. Navas, and D. Araujo, "Surface states of (100) O-terminated diamond: Towards other 1 × 1:O reconstruction models," *Nanomaterials*, vol. 10, no. 6, p. 1193, 2020. [Accessed: 31-Mar-2026].

[37] P. W. May and Yu. A. Mankelevich, "From ultrananocrystalline diamond to single crystal diamond growth in hot filament and microwave plasma-enhanced CVD reactors: A unified model for growth rates and grain sizes," *J. Phys. Chem. C*, vol. 112, pp. 12432–12441, 2008. [Accessed: 17-Mar-2026].

[38] R. Zulkharnay, "Electron emission studies of scandium on diamond for thermionic solar energy generation devices," Ph.D. dissertation, School of Physics, Univ. of Bristol, Bristol, U.K., Feb. 2023. [Accessed: 05-Apr-2026].

[39] Y. Ren, X. Li, W. Lv, H. Dong, Q. Cheng, F. Yue, N. Wöhrl, J. C. Mendes, X. Yang, and Z. Li, "Recent progress in homoepitaxial single-crystal diamond growth via MPCVD," *J. Mater. Sci.: Mater. Electron.*, vol. 35, p. 525, 2024. [Accessed: 20-Mar-2026].

[40] M. N. R. Ashfold, P. W. May, J. R. Petherbridge, K. N. Rosser, J. A. Smith, Y. A. Mankelevich, and N. V. Suetin, "Unravelling aspects of the gas phase chemistry involved in diamond chemical vapour deposition," *Phys. Chem. Chem. Phys.*, vol. 3, pp. 3471–3485, 2001. [Accessed: 27-Mar-2026].

[41] A. Cheesman, J. N. Harvey, and M. N. R. Ashfold, "Computational studies of elementary steps relating to boron doping during diamond chemical vapour deposition," *Phys. Chem. Chem. Phys.*, vol. 7, pp. 1121–1126, 2005. [Accessed: 14-Mar-2026].

[42] D. W. Comerford, A. Cheesman, T. P. F. Carpenter, D. M. E. Davies, N. A. Fox, R. S. Sage, J. A. Smith, M. N. R. Ashfold, and Yu. A. Mankelevich, "Experimental and modeling studies of B atom number density distributions in hot filament activated B_2H_6/H_2 and $B_2H_6/CH_4/H_2$ gas mixtures," *J. Phys. Chem. A*, vol. 110, pp. 2868–2875, 2006. [Accessed: 01-Apr-2026].

[43] University of Bristol, "Bristol NanoESCA Laboratory," School of Physics, University of Bristol. [Online]. Available: https://www.bristol.ac.uk/physics/facilities/nanoesca/. [Accessed: 24-Mar-2026].

[44] S. Ullah, G. Wan, C. Kouzios, C. Woodgate, M. Cattelan, and N. A. Fox, "Structure and electronic properties of tin monoxide (SnO) and lithiated SnO terminated diamond (100) and its comparison with lithium oxide terminated diamond," *Appl. Surf. Sci.*, vol. 559, p. 149962, 2021. [Accessed: 29-Mar-2026].

[45] D. Wolf, H. Jagodzinski, and W. Moritz, "Diffuse LEED intensities of disordered crystal surfaces. III. LEED investigation of the disordered (110) surface of gold," *Surf. Sci.*, vol. 77, pp. 265–282, 1978. [Accessed: 18-Mar-2026].

[46] U. Scheithauer, G. Meyer, and M. Henzler, "A new LEED instrument for quantitative spot profile analysis," *Surf. Sci.*, vol. 178, pp. 441–451, 1986. [Accessed: 02-Apr-2026].

[47] M. Nishitani-Gamo, K. P. Loh, I. Sakaguchi, T. Takami, I. Kusunoki, and T. Ando, "Surface morphology of homoepitaxially grown (111), (001), and (110) diamond studied by low energy electron diffraction and reflection high-energy electron diffraction," *J. Appl. Phys.*, vol. 86, no. 7, pp. 3740–3746, 1999. [Accessed: 16-Mar-2026].

[48] E. Maccallini, F. Siviero, A. Bonucci, A. Conte, P. Srivastava, and P. Manini, "Non evaporable getter (NEG) technology: A powerful tool for UHV-XHV systems," *AIP Conf. Proc.*, vol. 1451, pp. 24–27, 2012. [Accessed: 26-Mar-2026].

[49] F. A. Stevie and C. L. Donley, "Introduction to X-ray photoelectron spectroscopy," *J. Vac. Sci. Technol. A*, vol. 38, no. 6, p. 063204, 2020. [Accessed: 21-Mar-2026].

[50] H. Andrade, N. A. Fox *et al.*, "Use of energy-filtered photoelectron emission microscopy and Kelvin probe force microscopy to visualise work function changes on diamond thin films," *Int. J. Nanotechnol.*, vol. 11, no. 9–10, pp. 796–807, 2014. [Accessed: 04-Apr-2026].

[51] A. P. Baddorf *et al.*, "Identifying the secondary electron cutoff in ultraviolet photoemission spectra for work function measurements of non-ideal surfaces," *Sci. Rep.*, vol. 13, 2023. [Accessed: 15-Mar-2026].

[52] X. Gao, L. Liu, D. Qi, S. Chen, and A. T. S. Wee, "Water-induced negative electron affinity on diamond (100)," *J. Phys. Chem. C*, vol. 112, no. 5, pp. 1717–1721, 2008. [Accessed: 28-Mar-2026].

[53] B. P. Cairns, "Optimising the true negative electron affinity of lithium-oxygen-terminated diamond (110)," Final Year MSci Project Report, School of Physics, Univ. of Bristol, Bristol, U.K., 2025. [Accessed: 23-Mar-2026].

[54] O. A. Laput, I. V. Vasenina, A. G. Korzhova, A. A. Bryuzgina, U. V. Khomutova, S. G. Tuyakova, Y. H. Akhmadeev, V. V. Shugurov, E. N. Bolbasov, S. I. Tverdokhlebov, A. V. Chernyavskii, and I. A. Kurzina, "Effect of nitrogen arc discharge plasma treatment on physicochemical properties and biocompatibility of PLA-based scaffolds," *Polymers*, vol. 15, no. 16, p. 3381, 2023. [Accessed: 19-Mar-2026].

[55] S. Osswald, G. Yushin, V. Mochalin, S. O. Kucheyev, and Y. Gogotsi, "Control of sp^2/sp^3 carbon ratio and surface chemistry of nanodiamond powders by selective oxidation in air," *J. Am. Chem. Soc.*, vol. 128, no. 35, pp. 11635–11642, 2006. [Accessed: 30-Mar-2026].

[56] I. G. Enriquez, F. Muttaqien, M. Michiuchi, K. Inagaki, M. Geshi, I. Hamada, and Y. Morikawa, "Oxidative etching mechanism of the diamond (100) surface," *Carbon*, vol. 174, pp. 36–51, 2020. [Accessed: 17-Mar-2026].

[57] R. Yoshida, D. Miyata, T. Makino, S. Yamasaki, T. Matsumoto, T. Inokuma, and N. Tokuda, "Formation of atomically flat hydroxyl-terminated diamond (111) surfaces via water vapour annealing," *Appl. Surf. Sci.*, vol. 458, pp. 222–225, 2018. [Accessed: 03-Apr-2026].

[58] Argonne National Laboratory, "Lattice constants," Jan. 2025. [Accessed: 22-Mar-2026].

[59] M. Wang, N. Simon, C. Decorse-Pascanut, M. Bouttemy, A. Etcheberry, M. Li, R. Boukherroub, and S. Szunerits, "Comparison of the chemical composition of boron-doped diamond surfaces upon different oxidation processes," *Electrochim. Acta*, vol. 54, pp. 5818–5824, 2009. [Accessed: 25-Mar-2026].

[60] D. Petrini and K. Larsson, "Theoretical study of the thermodynamic and kinetic aspects of terminated (111) diamond surfaces," *J. Phys. Chem. C*, vol. 112, no. 8, pp. 3018–3026, 2008. [Accessed: 20-Mar-2026].

[61] S. Ullah, L. Cullingford, T. Zhang, J. R. Wong, G. Wan, M. Cattelan, and N. A. Fox, "An investigation into the surface termination and near-surface bulk doping of oxygen-terminated diamond with lithium at various annealing temperatures," *MRS Adv.*, vol. 6, pp. 311–320, 2021. [Accessed: 14-Mar-2026].

Certification of ownership of the copyright

This Project Report is presented as part of, and in accordance with, the requirements for the degree of MSci/BSc (delete as applicable) at the University of Bristol, Faculty of Science.

I hereby assert that I own exclusive copyright in the item named below. I give permission to the University of Bristol Library to add this item to its stock and to make it available for consultation in the library, and for inter-library lending for use in another library. I also give consent for this report to made available electronically to staff and students within the University of Bristol. It may be copied in full or in part for any bona fide library or research work. No quotation and no information derived from it may be published without the author's prior consent.

Author	Joseph Hynam
Title	Oxygen–Lithium Functionalisation of Boron-Doped C(110) Diamond for Low-Work Function NEA Surfaces
Date of submission	April 13, 2026

I agree that submission of this report constitutes signing of this declaration.

This project/dissertation is the property of the University of Bristol and may only be used with due regard to the rights of the author. Bibliographical references may be noted, but no part may be copied for use or quotation in any published work without the prior permission of the author. In addition, due acknowledgment for any use must be made.